Journal of Building Engineering 63 (2023) 105466

Contents lists available at ScienceDirect

Journal of Building Engineering

journal homepage: www.elsevier.com/locate/jobe

Optimal position of air purifiers in elevator cabins for the improvement of their ventilation effectiveness

Luis Santamaría Bertolín [a], Jesus Manuel Fernández Oro [a,*], Katia Argüelles Díaz [a], Mónica Galdo Vega [a], Sandra Velarde-Suárez [a], María Elena Del Valle [b], Luis Joaquín Fernández [b,**]

[a] Fluid Mechanics Area, Department of Energy, University of Oviedo, C/ Wifredo Ricart, s/n, Gijón, Asturias, 33204, Spain
[b] TK Elevator Innovation Center, La Laboral, C/ Luis Moya Blanco 261, Gijón, Asturias, 33203, Spain

ARTICLE INFO

Keywords:
Mean age of air
Elevator cabin
Ventilation
Infiltration
Purifier
COVID-19

ABSTRACT

Ventilation in confined spaces is essential to reduce the airborne transmission of viruses responsible for respiratory diseases such as COVID-19. Mechanical ventilation using purifiers is an interesting solution for elevator cabins to reduce the risk of infection and improve the air quality. In this work, the optimal position and blowing direction of these devices to maximize ventilation and minimize the residence time of the air inside two cabins (large and small) is studied. Special attention is devoted to idle periods when the cabin is not used by the passengers, in order to keep the cabin ambient safe and clean, avoiding that the trapped air in the cabin (after its use) could suppose a reservoir for contaminants. CFD numerical models of two typical cabin geometries, including the discretization of small slots and grilles for infiltration, have been developed. A full 3D URANS approach with a k-epsilon RNG turbulence model and a non-reactive scalar to compute the mean age of air (MAA) was employed. The CFD results have been also validated with experimental measurements from a home-made 1:4 small-scale mock-up. The optimal position of the purifier is on the larger sidewall of the cabins for a downward blowing direction (case 1 of the database). Flow rates in the range of 0.4–0.6 m^3/min, depending on the size of the cabin, are sufficient to assure a correct ventilation. Upward blowing may be preferable only if interaction of the jet core with the ceiling or other flow deflecting elements are found. In general, the contribution of infiltrations (reaching values of up to 10%), and how these secondary flows interact with the main flow pattern driven by the purifier, is relevant and not considered previously in the literature. Though an optimal position can improve ventilation considerably, it has been proven that a good choice of the purification flow rate is more critical to ensure an adequate air renewal.

1. Introduction

The emergence of COVID-19 has brought back into focus the importance of airborne transmission for the spread of viruses and other respiratory diseases. Proper ventilation in confined spaces is essential to drastically reduce possible viral loads in the environment and thus minimizes the risk of airborne infection for people [1–3]. In particular, mechanical ventilation systems ensure the replacement of polluted air and renew the quality of the environment through the injection of fresh air from the outside.

* Corresponding author.
** Corresponding author.
E-mail addresses: jesusfo@uniovi.es (J.M. Fernández Oro), luis-joaquin.fernandez@tkelevator.com (L.J. Fernández).

https://doi.org/10.1016/j.jobe.2022.105466
Received 19 July 2022; Received in revised form 18 October 2022; Accepted 22 October 2022
Available online 2 November 2022

Elevator cabins are confined spaces with small dimensions and high occupancy rates that are particularly susceptible to air renewal problems. They do not usually incorporate any assisted ventilation element, so air renewal is mainly produced by the simple opening of the cabin each time passengers are loading or unloading. Only reduced ventilation grilles and openings provide some minimum ventilation rates when doors are closed. Under certain operating conditions, the cabins can become reservoirs of viral loads acting as transmission sources [4–8]. Hence, the incorporation of additional ventilation systems in the cabins is an ideal solution to guarantee the safety of users [9,10].

Leading cabin manufacturers (OTIS, TK Elevator, MitsubishiElectric, among others) are beginning to incorporate air conditioning systems to ensure a safe, virus-free atmosphere. These include ionizers and UV light generators, able to remove viruses from the fluid stream but still in the validation phase [11–14]. A more reliable and mature solution is the introduction of mechanical purifiers, which are able to trap possible viral loads suspended in the environment through high retention HEPA and/or ultra-HEPA filters [15–18].

In order to maximize the performance of these purifiers, it is essential to choose an optimal position for their installation. It must be guaranteed that renewal times are minimized and overall ventilation patterns are favored. In general, they should interact positively with the existing infiltrations in the cabin through the grilles and slots, hence maximizing the overall ventilation and eliminating dead volumes. The choice of the blowing direction, the point of emission of the purified air, as well as the operating parameters (activation time, flow rate injected) must be also properly selected.

At present time, the amount of works analyzing the ventilation effectiveness in elevator cabins is quite reduced in the scientific literature. Recent works have employed CFD methodologies to analyze thermal comfort of passengers, showing that mechanical systems can enhance the ventilation and control the temperature inside the cabin. Typical velocities around 0.5 m/s for temperature rise of 12 °C between the passengers and the ambient were simulated [19]. Complementarily, in the context of COVID 19 pandemic, experimental works have also demonstrated the need for additional ventilation, pointing out that downflow ventilation is key to guarantee healthy and safe air conditions [20]. Concentrations of virus particles can hover in the elevator cabin up to 20 min after use [21], so mechanical ventilation should be working for long periods of time to be effective. Moreover, active particle control technology (purifiers) can reduce contamination and aerosolized bioburden through effective air purification [22], requiring important renovation flowrates. More recently, Nouri et al. have determined that aerosol disinfectant combined with air conditioning is mandatory to reduce the number of infected particles by COVID-19 and control the disease spreading [23].

The study of indoor air quality inside elevators can be approached macroscopically by analyzing the behavior of the flow patterns and evaluating the age of the air inside the cabins. Although there are not many elevator-specific works in the literature, references are found for similar situations including ventilation in offices, in enclosed rooms or in aircraft cabins [24–27]. The ASHRAE standards [28,29] define a series of metrics to determine whether the existing ventilation guarantees the effectiveness of the system. To apply this methodology, a series of tracers must be used to estimate, on average, the residence time of the confined air volume in the elevator. Experimentally, the references analyzed show that it is not possible (or it is very expensive and very limited) to perform reliable tests to monitor the behavior of suspensions of particles with viral loads at long times (only works showing the behavior of mists and/or droplets by means of visualization techniques, associated with sneezing and coughing, at short times after emission are available). Consequently, numerical methods have emerged as an ideal tool for the study of this type of flows that are difficult to characterize in the laboratory.

With CFD numerical tools, it is possible to simulate the evolution of particles of different microscopic sizes (distributions of different diameters) that are expelled from an emitting point. Lagrangian particle methods, typically DPM, where particles are passively transported by the bulk flow (i.e., assuming that they are sufficiently diluted and cannot modify the streamlines) provide very interesting results, despite being computationally expensive simulations and with difficult overall extrapolations. On the contrary, the evaluation of global flow patterns and the characterization of numerical tracers, either in the form of residence curves (RTD) or spatial age of air distributions (MAA), offer a sufficient description of the overall performance of the ventilation system; especially if the interest is devoted to compare different operating scenarios that determine the optimal solution [30–32].

In this work, the optimal position and blowing direction of a standard air purifier inside a typical elevator cabin has been studied. Two typical cabins have been considered for the purpose, manufactured by TK Elevator and called Evolution (EVO) and Synergy (SYN). They correspond respectively to cabins for intensive use, for large service buildings such as hospitals; and smaller cabins as those found in residential buildings. This work is part of the project "INN-MEDICAL: Innovative Medical Industry enabling an Efficient and Autonomous response against COVID-Like Pandemic", a multidisciplinary R&D consortium to promote pandemic protocols for hospital centers.

For the study, a three-dimensional model of the cabins has been developed, with sufficient detail to discretize the grilles and the small gaps between the cabin and the elevator shaft, on which the unsteady flow governing equations have been solved. In terms of limitations and restrictions for the study, neither the modelling of heat transfer, nor the volume occupied by the passengers have been considered systematically (a detailed discussion of their relevance in the present numerical database is provided in section 2). Although some works emphasize the importance of the effects associated with the volume occupied by people on ventilation patterns, these usually have a greater impact when they are in motion [33–35]. In the case of elevator cabins, travelers have an obvious limitation of movement so their effect will be reduced. Furthermore, as the work focuses on the analysis of different position configurations of the purifier, the effect of introducing solid bodies simulating the occupancy of people is assumed to have a similar (minor) blocking effect in all cases, so it has been chosen not to model them. In addition, it would be arbitrary to consider an occupation of the cabin with one or several people, or even one of them blocking the air outlet of the purifier with his/her body, forcing an impracticable number of simulations.

The results obtained have allowed concluding which is the optimum position of the air purifiers in each cabin, indicating also the most advisable blowing direction. The operating parameters of the purifiers have also been contrasted and characteristic air renewal

times are provided in the most sensitive areas related to passenger occupancy.

2. Numerical methodology

2.1. General background

A three-dimensional model of the cabins has been developed, with sufficient detail to model the grilles and the small gaps between the cabin and the elevator shaft, on which the unsteady RANS equations have been resolved using the commercial software ANSYS Fluent v16.2. For the computation of the mean age of air in the cabins, a User-Defined Scalar (UDS) has been defined with a unit source term in the whole domain to calculate the accumulated elapsed time for the fluid. Additionally, in order to correctly characterize the pressure losses associated with the cabin grilles, complementary models have been built to simulate the air flow through the grilles, obtaining the evolution of each loss coefficient for different Reynolds numbers (different flow velocities). These values have been introduced in the elevator model to regulate the infiltration flows with the exterior, using an iterative procedure to calibrate the final value of the coefficients as a function of the flow regime established in the grilles.

2.2. Basic cabin geometries

The inside areas of two elevator cabins manufactured by TK Elevator (TKE) have been modelled numerically. The first cabin, designed for elevators installed in public service buildings (hospitals, administrative buildings, etc.), is the Evolution (EVO) cabin, with a load capacity of up to 20 passengers (maximum load of 1600 kg) and an effective volume of 7.4 m^3. The second cabin, the Synergy cabin (SYN), is for use in residential areas, with a maximum capacity of 8 passengers (maximum load of 630 kg) and a practicable volume of 3.4 m^3.

2.2.1. Cabin geometrical parameters

The basic dimensions of the cabins are presented in Table 1. An overview of these cabin is shown in Fig. 1 (up).

The EN 81-1 standard [36] (as similar American regulations [37]) establishes a series of minimum ventilation requirements based on the presence of openings and perforations that prevent the cabins from being hermetic. In particular, the cabins must have perforations in both upper and lower parts of the car, with a value of at least 1% of the cabin floor area in each zone (therefore 2% on aggregate). In addition, the gaps and slots around the cabin are allowed to represent half of this total area.

Table 2 shows the values of the perforations (in the form of grilles) made in the EVO cabin to guarantee the existence of these infiltrations, in relation to the total floor area of the cabin ($140 \times 240 = 33{,}600$ cm^2). The percentage of effective cross-section for these grilles is given in brackets. In addition, the cross-sections of the small slots and gaps of the doors, typically with a clearance of about 4 or 5 mm, are also provided. The total infiltration area for the EVO cabin is about 3% of the cabin floor area.

In the case of the SYN cabin, infiltrations are more concentrated through a series of lateral grilles, with gaps only in the area of the cabin doors. In this case, the total infiltration surface area represents 3.2% of the total area of the cabin floor ($110 \times 140 = 15{,}400$ cm^2), see Table 3.

Fig. 1 (down) shows a detail of the grilles zones and gaps associated with the clearances of the EVO cabin. On the right, it is shown the simplification of the geometry to be modelled numerically, indicating the location of these slots (enlarged slot sections, not-to-scale). The sketch on the right also shows the placement of the air purifier (small box near the ceiling) on the right sidewall of the cabin.

2.2.2. Air purifier geometrical parameters

Six possible positions of the air purifier in the elevator cabin have been considered for the study. These positions have been chosen considering a series of practical restrictions for their installation: location in areas accessible to installers, at a certain height (at least 1.75 m above the cabin floor) to avoid undue manipulation by passengers -mainly children-, avoiding areas affected by lights, button panels, etc., and preserving constructive elements of the cabins according to the manufacturer guidelines. Therefore, up to 12 different cabin models have been generated (6 models for the EVO cabin and another 6 for the SYN cabin), placing the air purifier in the positions shown in Fig. 2. Positions 1 and 2 shown in the figure correspond to the sidewall (centered and bottom); positions 3 and 4 are on the backwall (centered and side) and positions 5 and 6 are azimuthal positions with longitudinal or transversal placement of the purifier. In addition, the downward direction has been selected as the preferred blowing direction (following recommendations found in the bibliography [19,20]), although inverted blowing situations have also been tested (see results later).

The purifier has been modelled as a parallelepiped, with maximum dimensions $168 \times 93 \times 275$ mm, according to the supplier's specifications. The purifier consists of 3 filtering stages (pre-filtering, adsorption and ultra-efficiency filtering) and a small intermediate fan that generates the required recirculation flowrate. The blowing and suction sections of the purifier are 120×65 mm.

2.2.3. Operating parameters

Table 4 shows the operating conditions of the air purifiers for the two cabin geometries considered. Note that the internal flow in

Table 1
Cabin geometrical dimensions.

Dimensions	*EVO cabin*	*SYN cabin*
Width (mm)	1400	1100
Length (mm)	2400	1400
Height (mm)	2200	2200

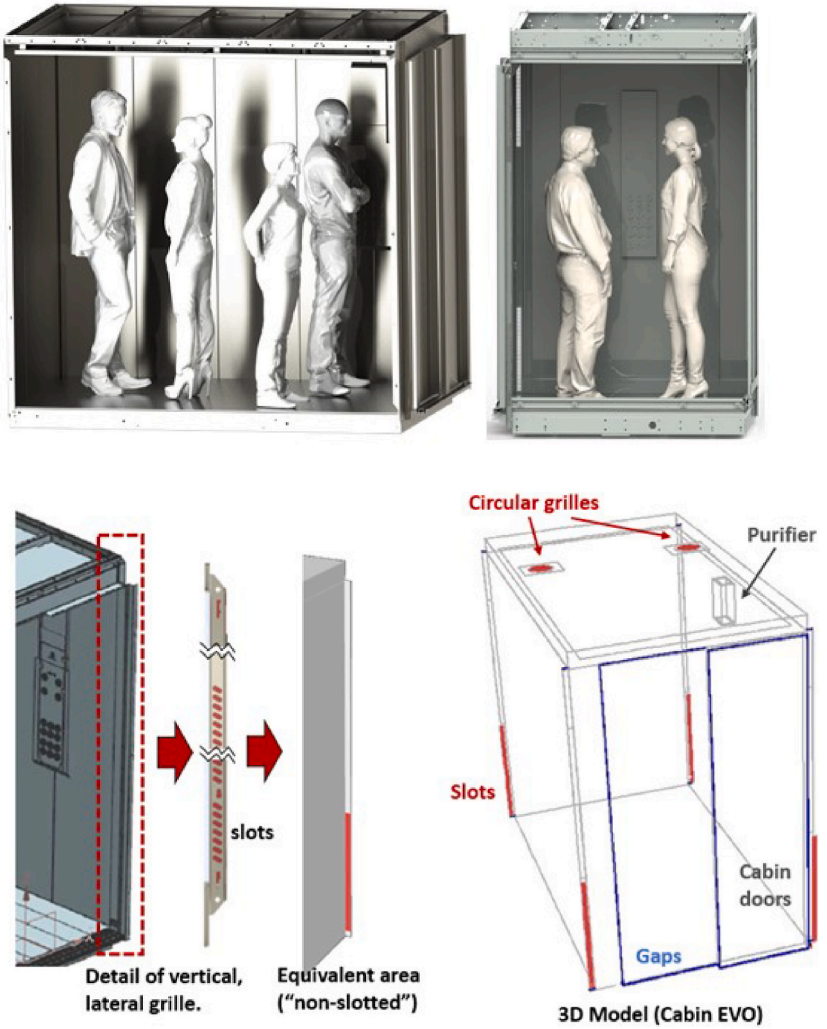

Fig. 1. Models of the EVO (left, up) and SYN cabin (right, up). Details of the lateral grilled zone (left, down) and modelling of infiltrations: grilles, in red, and gaps and slots, in blue (right, down). (For interpretation of the references to color in this figure legend, the reader is referred to the Web version of this article.)

Table 2
Opened areas to ensure infiltrations in the EVO cabin.

Elements	Position	Area (cm^2) [1]	Total effective area (cm^2) [2]
Circular grilles	Ceiling	349 (48%)	660 (1.96%) [3]
Rectangular grilles	Floor	29 (31%)	
Vertical grilles	Sidewalls	968 (50%)	
Upper slots	Ceiling	48 (100%)	362 (1.07%)[3]
Lower slots	Floor	64 (100%)	
Door gaps	Sidewalls	250 (100%)	

[1] Total grilles area, indicating in % the proportion of free opening (without louvers).
[2] Aggregate opening sections for air infiltration.
[3] Percentage with respect to cabin floor area (33,600 cm^2).

the purifiers will not be simulated numerically, since the interest of the study is focused on the ventilation conditions of the elevator cabins. Therefore, the purifiers simply represent both air inlet and outlet sections to the domain. The selection of the operating flow rate in each geometry has been made to ensure a minimum rate of at least 5 air renewals per hour in the cabins, as indicated by the project baseline data, which is coherent with similar guidelines of references [21,22].

Table 3
Opened areas to ensure infiltrations in the SYN cabin.

Elements	Position	Area (cm^2) [1]	Total effective area (cm^2) [2]
Circular grilles	Ceiling	258 (50%)	266 (1.72%) [3]
Rectangular grilles	Floor	274 (50%)	
Upper slots	Ceiling	18 (100%)	226 (1.46%)[3]
Lower slots	Floor	48 (100%)	
Door gaps	Sidewalls	160 (100%)	

[1] Total grilles area, indicating in % the proportion of free opening (without louvers).
[2] Aggregate opening sections for air infiltration.
[3] Percentage with respect to cabin floor area (15,400 cm^2).

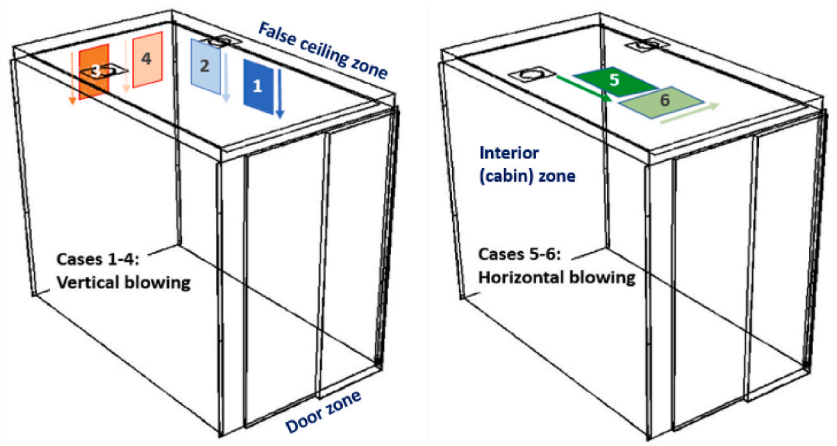

Fig. 2. Sketch showing the positions considered for the air purifier in the case of EVO cabin (similar in the case of SYN cabin).

Table 4
Operating conditions of the air purifier in the cabins.

	EVO cabin	SYN cabin
Flow rate (m^3/min)	0.6	0.4
Blowing velocity (m/s)	1.30	0.85
Turbulence level (%)	5.0	5.0
Reference time (s)	740	510

2.3. Cabin mesh and grid distributions

The extremely reduced cross-sections for the flow infiltration complicate (and make very expensive) the generation of an accurate mesh in those regions. In addition, the presence of secondary elements in the geometry, such as false ceilings, uneven steps and doors corners, or the air purifier itself, implies the intersection of different mesh distributions, making the construction of a single conformal

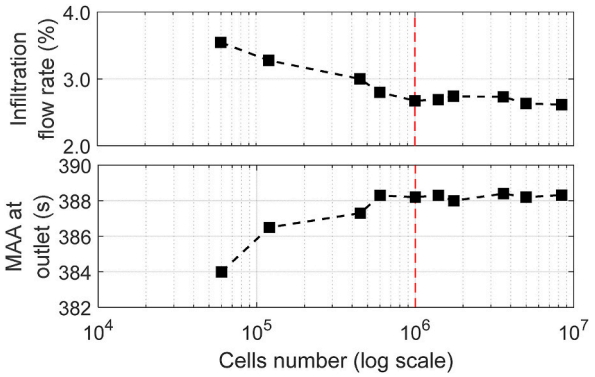

Fig. 3. Mesh sensitivity analysis (SYN cabin): local effect of the mesh in the infiltration rates (up) and global effect in the estimation of the mean age of air (down).

mesh impracticable. To solve this drawback, several interfaces have been incorporated into the model, separating the simulation geometry of each cabin into three blocks: false ceiling area, door area and interior area (real occupancy volume).

Taking advantage of the rectangular shape of the cabins, it has been possible to introduce a structured Cartesian mesh (not equidistant), stacking the mesh against the walls for a better description of the flow gradients in such air boundary layers. A maximum y^+ value around 5–7 has been guaranteed on all cabin walls (including the smallest gaps), thus ensuring a good resolution of the flow patterns in the most sensitive areas.

A mesh sensitivity analysis has been conducted over a slight simplified model of the SYN cabin for simplicity in the mesh generation (only considering the vertical gaps of the doors but maintaining the main features of the purifier). In Fig. 3, the percentage of the infiltration flow rate with respect to the purifier flow rate is given as a function of the cells number, showing that a typical mesh density over 1.0 million cells for the whole cabin is sufficient to provide a convergent value of the local infiltrations (it already maintains the numerical uncertainty below irrelevant differences). Note that stacking the mesh against the walls is essential to get accurate results (preserving y + around 7 in all the situations) so the flow in the gaps can be resolved with sufficient fidelity. Fig. 3 also reveals that the computation of the mean age of air is quite unresponsive to the mesh size, with marginal differences even below 1% for the coarser meshes.

Finally, the total number of cells used was 2.1 million cells for the EVO cabin and 2.0 million cells for the SYN cabin. Fig. 4 shows a detail of the mesh used, generated from the meshing generation program GAMBIT.

Note that an extra overset mesh configuration has been also developed to simulate the influence of the cabin occupancy in the results. In particular, two mannequins within the SYN cabin have been discretized with a 5 mm mesh size on the body surfaces and enclosed by an auxiliary volume. A total number of 0.55 million cells were adopted for this secondary domain (more details in section 2.8).

2.4. Grille modelling

In the case of the grilles modelling, it is not feasible to introduce their exact geometry (with all the detailed slots that compose them) in the complete model of the cabin. The disparity of scales, between the global volume of the elevator and the existence in some cases of more than 60 small steel plates per grille, make it impossible to simulate them together with practical computational resources. Instead, the geometries of the existing grilles in the cabins have been simulated independently, in order to characterize their dynamic fluid behavior at very low Reynolds numbers (the air flow velocities through these grilles will be significantly small, just a few cm/s). Note that special care is necessary because we need to know their behavior in the transition zone from turbulent to laminar flow. Afterwards, the characterization of the loss coefficient of these louvers will be used as a boundary condition for the equivalent surfaces considered in the general model of the cabins.

It is very important to obtain a good characterization of these elements, since they drastically dictate the infiltration flow rates established in the cabins based on the small pressure differences between the inside and the outside. It is not advisable, therefore, to assign them a turbulent quadratic loss relating the head loss in the grilles as a function of the infiltration flow rate. Since this is valid only at moderate or high Reynolds numbers in the case of ducted flow, it is therefore necessary to analyze in detail their behavior over a wider range of velocities.

For that purpose, three different grille models have been completed, according to the existing arrangements in both EVO and SYN cabins. Specifically, three additional numerical models have been developed, all of them incorporating progressive meshing:

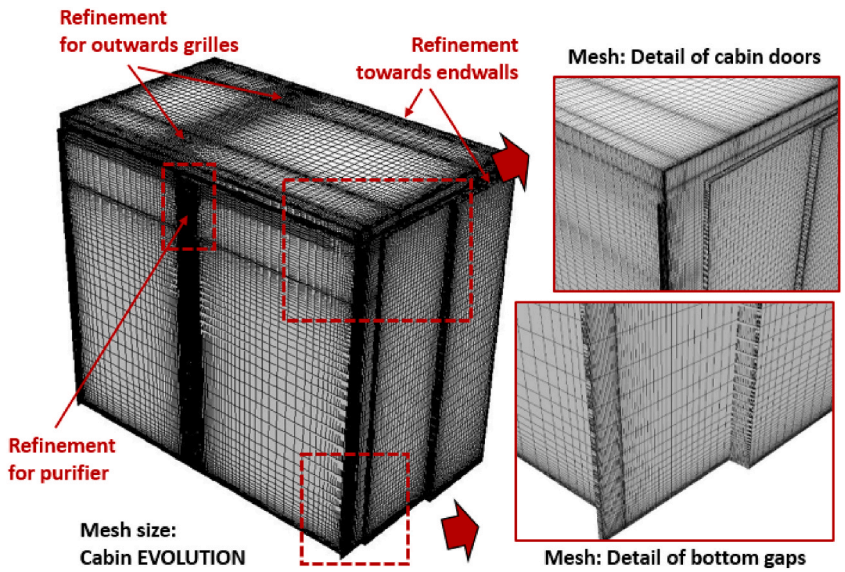

Fig. 4. A) Overall view of the mesh for the EVO cabin. B) Discretization details in the doors area (the width of the lateral grids is identified).

a) An axisymmetric and three-dimensional periodic model of a circular grille with 5 louvers and 36° of circumferential periodicity. It is equivalent to an effective air opening of a 48.3% for a hydraulic diameter of 150 mm. This type of circular grille is installed on the EVO cabin roof (two of them). It has been simulated with 1.73 million cells.
b) A longitudinal and three-dimensional model of a rectangular grille with 4 louvers, 60 mm in span and 9 mm spacing between the louvers, resulting in a 30.9% of effective air opening for a hydraulic diameter of 48 mm. This rectangular grille, which is used on the sidewalls of the EVO cabin doors, has been simulated with 1.35 million cells.
c) A longitudinal and three-dimensional periodic model of 1 single louver, 8 mm span and 4 mm gap between louvers, corresponding to a 50% effective air opening, for a hydraulic diameter of 50 mm. This type of extended grille, which covers up to 480 mm in span and includes 60 louvers, appears on the sidewalls of the SYN cabin doors and also on the side closing folds of the EVO cabin (Fig. 1, down right). It has been simulated with 1.35 million cells.

Fig. 5 shows the details of these grille models. On the left, a global view of the domains with the identification of the boundary conditions is shown; while a detail of the mesh discretization used is shown on the right. To obtain the grilles behavior for a wide range of Reynolds numbers, steady simulations have been performed for 9 different values of the inlet velocity, from 0.1 mm/s to 5 m/s. Hence 27 cases in total have been executed to obtain an accurate fluid dynamic description of these elements. To determine the pressure drop across the grilles, the average pressure values at a typical distance of one half of the hydraulic diameter, both upstream and downstream of the grilles, were used. Table 5 shows the results obtained for the loss coefficient of each grille, defined as: $K_L = 2\Delta p/\rho v^2$.

Note that at high velocities through the grilles (greater than 0.5 m/s), the flow established is already turbulent, so the simulations were solved using a k-ε RNG turbulence model for the RANS methodology. Fig. 6 shows graphically the results summarized in Table 6. In addition, an example of the flow established in both circular and rectangular grilles is shown, for the case of a laminar flow with a velocity of 10 cm/s (corresponding to the expected values for the operation of the grilles in the cabins).

As expected, the loss coefficient is extremely influenced by the flow regime, which clearly justifies the approach adopted. Although no published values are available in the specific literature to contrast the results obtained at low Reynolds numbers, contrast values are shown at high Reynolds numbers (when the coefficient turns to be insensitive to Reynolds number variations, taken from Ref. [38]). They are shown in the figure as single points for grilles with equivalent opened cross-sections. These references fit perfectly with the

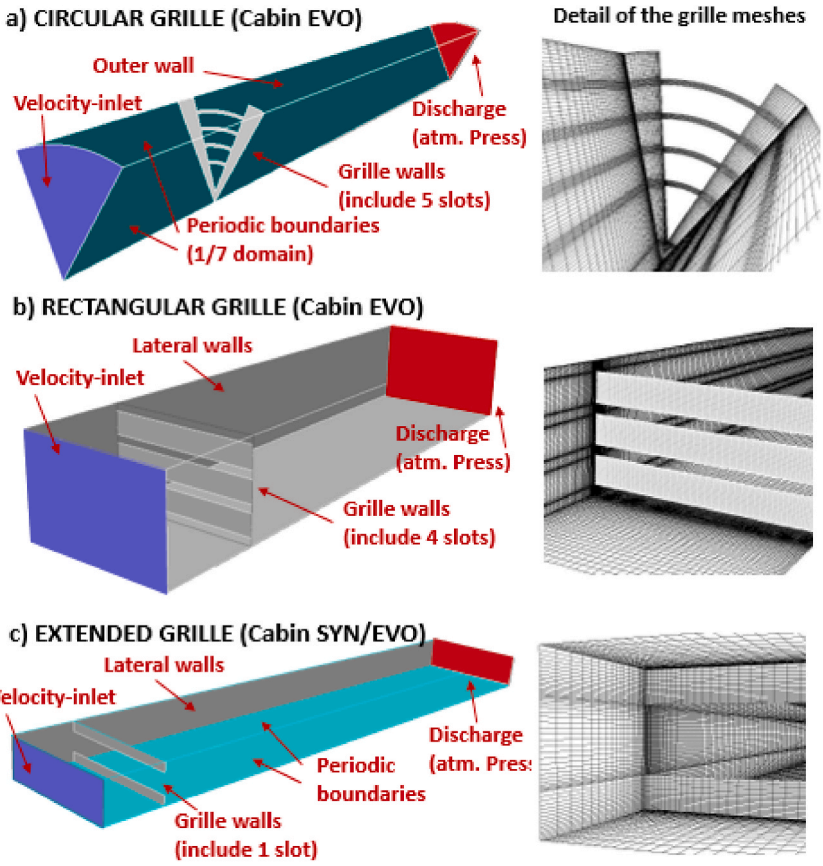

Fig. 5. Simulation domains for the individual grilles. a) Circular grille in EVO cabin. b) Rectangular grille in EVO cabin. c) Extended grille in EVO/SYN cabins. On the left, simulation domains; on the right, detail of the meshes used.

Table 5
Results for the independent simulations of the grilles.

Cases & Model		1. Circular grille		2. Rectangular grille		3. Extended grille	
Velocity (m/s)	Simulation type	Re	K_L	Re	K_L	Re	K_L
5.0	k-ε RNG	51100	5.00	16073	18.0	17114	5.01
1.0	k-ε RNG	10200	5.03	3214	18.3	3422	5.04
0.5	k-ε RNG	5100	5.11	1607	18.8	1711	5.07
0.1	Laminar	1020	5.86	321	20.5	342	5.81
0.05	Laminar	510	6.72	160	22.6	171	6.38
0.01	Laminar	102	10.8	32	46.0	34	17.9
0.005	Laminar	51	17.3	16	79.8	17	33.9
0.001	Laminar	10.2	77.6	3.2	385.4	3.4	165.1
0.0001	Laminar	1.0	776.4	0.3	3851	0.3	1645

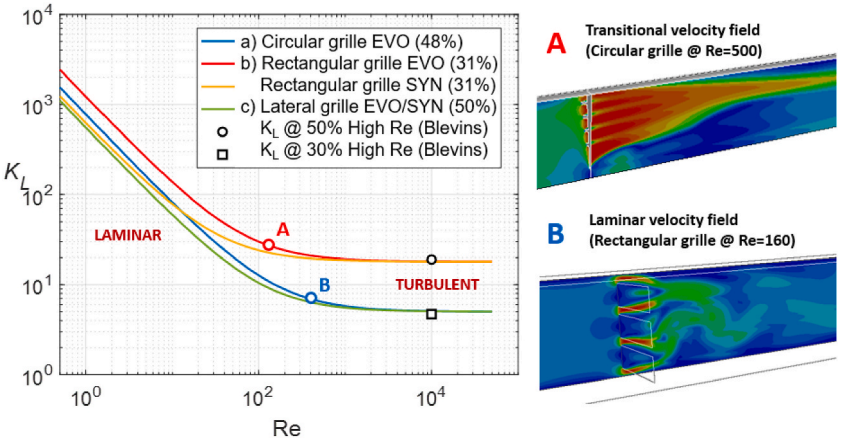

Fig. 6. Characterization of the grilles performance. A) Results for the circular grille at 0.1 m/s (laminar flow). B) Results for the rectangular grille at 0.1 m/s (laminar flow).

Table 6
Comparison on averaged mean ages of air in the SYN cabin between empty and occupied scenarios.

	MAA [s]					
Zone "Cabin"	C1	C2	C3	C4	C5	C6
Cabin with passengers (Occupied)	310	329	326	316	298	329
Cabin without passengers (Empty)	350	363	352	353	335	404
Difference (%)	11.4	9.4	7.4	10.5	11.0	18.6

values obtained in our simulations.

2.5. General numerical modelling

The full 3D model of the cabins has been implemented in the ANSYS-FLUENT solver to resolve the unsteady RANS equations using a k-ε RNG turbulence model. It was assumed incompressible, viscous flow of air at standard atmospheric conditions. Thermal effects, due to buoyancy or heat transfer, have been neglected according to similar works for confined flows in the literature [39]. The whole set of equations is:

- Continuity equation:

$$\frac{\partial \overline{u}_i}{\partial x_i} = 0 \tag{1}$$

- Momentum equation (Navier-Stokes):

$$\rho \frac{\partial \overline{u}_i}{\partial t} + \rho \frac{\partial \left(\overline{u}_i \overline{u}_j\right)}{\partial x_j} = -\frac{\partial \overline{p}}{\partial x_i} + \mu \nabla^2 \overline{u}_i + \frac{\partial \tau_{ij}}{\partial x_j} \tag{2}$$

Where the Reynolds Stress Tensor in the momentum equation has been modelled using an Eddy Viscosity Model, according to:

$$\tau_{ij} = -\rho\overline{u_i' u_j'} = \mu_t \underbrace{\left(\frac{\partial \overline{u}_i}{\partial x_j} + \frac{\partial \overline{u}_j}{\partial x_i}\right)}_{S_{ij}} - \frac{2}{3}\rho k \delta_{ij} \tag{3}$$

being $= \frac{1}{2}\rho\overline{u_k' u_k'}$, the turbulent kinetic energy and $\mu_t = \rho C_\mu \frac{k^2}{\varepsilon}$, the turbulent viscosity, with $C_\mu = 0.0845$. Moreover, the turbulence closure has been considered using a two-equation k-epsilon RNG turbulence model, because of its robustness and versatility. In this case, these equations are (neglecting buoyancy):

$$\rho\frac{\partial k}{\partial t} + \rho\frac{\partial (k\overline{u}_i)}{\partial x_i} = \frac{\partial}{\partial x_j}\left[\alpha_k \mu_t \frac{\partial k}{\partial x_j}\right] + 2\mu_t S_{ij} S_{ij} - \rho\varepsilon \tag{4}$$

$$\rho\frac{\partial \varepsilon}{\partial t} + \rho\frac{\partial (\varepsilon\overline{u}_i)}{\partial x_i} = \frac{\partial}{\partial x_j}\left[\alpha_\varepsilon \mu_t \frac{\partial \varepsilon}{\partial x_j}\right] + C_{\varepsilon 1}\frac{\varepsilon}{k}\left(2\mu_t S_{ij} S_{ij}\right) - \rho C_{\varepsilon 2}\frac{\varepsilon^2}{k} \tag{5}$$

Where the turbulent dissipation rate is defined as $\varepsilon = 2\nu\overline{s_{ij}' s_{ij}'}$, being $s_{ij}' = \frac{1}{2}\left(\frac{\partial u_i'}{\partial x_j} + \frac{\partial u_j'}{\partial x_i}\right)$; and typical coefficients $C_{\varepsilon 1} = 1.42, C_{\varepsilon 2} = 1.68$ and $\alpha_k = \alpha_\varepsilon \sim 1.383$ have been employed.

The equations have been discretized using the finite volume method with a second-order upwind scheme for the spatial convective terms. Green-Gauss cell-based method for the computation of the spatial gradients over the diffusion terms in the momentum equation was also selected. In addition, a second-order discretization scheme has been employed for the transport equations of the turbulent kinetic energy and the turbulent dissipation rate of the turbulence model. The discretization of the temporal terms (when necessary) is also of second-order accurate. For the pressure-velocity coupling, a classic SIMPLE algorithm has demonstrated a sufficient compromise between stability and CPU time. A convergence criterion of 10^{-5} was fixed for the continuity equation, with a minimum threshold of 10^{-4} for all the equations resolved. Default relaxation factor have been maintained in all cases (0.3 and 0.7 for pressure and momentum equations and 0.8 for turbulent transport equations).

In addition, according to the level of refinement employed in the mesh of the wall adjacent cells, the scalable option has been selected as the most appropriate wall function [40]. This wall treatment formulation is recommended for meshes having values of y+>1 but below the transition zone between the viscous sublayer and the fully turbulent outer layer (y+<11). This selection matches perfectly with the stacking grid distribution adopted in the sidewalls of the cabins (section 2.3), especially for the surfaces representing the smaller grilles and slotted gaps.

Complementarily, to track the mean age of air unsteadily in the elevator cabin, an additional transport equation has been defined for a non-reactive scalar. The equation governing this scalar follows the classic conservative expression:

$$\rho\frac{\partial \varphi}{\partial t} + \frac{\partial}{\partial x_i}\left[\rho\overline{u}_i\varphi - \Gamma\frac{\partial \varphi}{\partial x_i}\right] = S_\varphi \tag{6}$$

where Γ y S_φ are, respectively, the diffusion coefficient and the source term for the scalar φ representing the mean age of air. It has been also resolved with a second-order upwind discretization for a convergence criterion of 10^{-6} and relaxation factor equal to unity. The diffusion coefficient for the molecular transport is given by the equation proposed in Refs. [41,42], which is widely accepted as a good approximation of the diffusive effects in air:

$$\Gamma = 2.88 \cdot 10^{-5}\rho + \mu_t / 0.7 \tag{7}$$

Note that this formulation must introduce a unit source term for all the cabin volume ($S_\varphi = 1$), so that the scalar is directly accounting for the cumulative time that has elapsed since the renewed air is injected from the purifier in the unsteady computations.

2.6. Boundary conditions

The following boundary conditions have been defined in the CFD model of the cabins: (1) the air inlet coming from the purifier, as "velocity-inlet" (see values introduced in Table 4 above); (2) the air outlet (purifier suction), as "velocity-outlet" (with the same negative value that guarantees the global mass conservation due to the equal-sized areas of both inlet and outlet sections) and (3) atmospheric pressure conditions ("pressure-outlet" equal to zero, in relative terms) in all the gaps and slots connected to the outside. Additionally, the grilles are defined as (4) outlet-vent boundary conditions, which introduce a loss coefficient, equivalent to the K_L obtained above. Finally, the rest of the solid walls and contours are defined as (5) stationary wall condition. As mentioned earlier, the models also incorporate interfaces connecting the different blocks of the domain (door zone, false ceiling zone and occupancy zone).

For the scalar representing the mean age of air, a condition with a zero value is set at the entrance of the domain from the purifier. By imposing this condition, it is assumed that the air that is recirculated to the interior, and that has just been sanitized in the purifier, accounts as a fully renewed air, and with a quality like the outside air coming from the infiltrations. Similarly, the pressure-outlet conditions impose a zero-valued boundary for the scalar, assuming that the incoming air from the outside is completely renewed air (and, therefore, of zero initial age). Finally, in the velocity-outlet condition, a zero flux boundary condition is set, ensuring that there are no longer diffusive effects of the scalar through the outlet, but with an age of air value that it is preserved to be convected

towards the purifier.

2.7. Solution procedure, numerical stability, and convergence

Once the basic parameters, simulation models and boundary conditions of the problem have been set, the numerical procedure to complete the required simulation program must be defined. Each of the 6 cases simulated per cabin has been solved following a procedure comprising these two stages:

- Stage 1: Steady simulation of the internal flow in the cabins (closed doors), because of the inlet jet generated by the air purifier. This type of simulation solves the flow equations and the turbulent variables in a steady fashion until the final asymptotic solution is obtained. Note that, to obtain this final field, it was necessary to perform an additional iterative process over the value of the loss coefficient in the grilles. It was started assuming loss coefficients corresponding to fully turbulent regime (the high Reynolds number case). Typically, 2 to 3 intermediate simulations per case were necessary to determine the final K_L value fitted to the operating conditions.
- Stage 2: The transport equation for the mean age of air is activated, while further resolution of the flow equations is now set off, in order to save computational resources. This allows the unsteady resolution of the scalar equation inside the cabin on the basis of the flow field solved in the previous stage. Since the flow patterns have already reached their steady state at the end of stage 1, it is possible to deactivate the resolution of the flow equations and only resolve the transport (convective and diffusive) of the scalar in the permanent flow field. This unsteady evolution has been resolved for 3600 s, assuring that the mean age of air distribution has also reached its own steady state. Time steps in the order of $\Delta t = 1$ s have been chosen for the computation of the temporal terms.

The results of both stages are used to judge, in both cabins, which of the six positions is the most advantageous for a better ventilation under minimum values of mean age of air.

2.8. Validation and modelling restrictions

2.8.1. Experimental validation

To validate the numerical modelling, we have constructed a 1:4 small-scale mock-up of the SYN cabin to reproduce the air flow patterns in the real elevators for some representative cases. In particular, cases 1 and 3 corresponding to the air purifier placed in the lateral sidewalls and blowing downwards have been considered for validation. To preserve similarity between the real geometry and the small-scale model, Reynolds and Strouhal numbers are maintained.

The preservation of the Reynolds number for the scaled model at the lab (Re^*) provides the following relationship for the velocity: $v^* = v/\lambda_L$; or, in terms of flow rate, $Q^* = Q\,\lambda_L$. Consequently, for a reduced scale 1:4 ($\lambda_L = 1/4$), the flow rate fixed in the model (0.1 m^3/min) is four times lower than in the real cabin (0.4 m^3/min). On the other hand, keeping similarity for the Strouhal number ($St = St^*$), the new reference time for the air renewal in the mock-up is obtained as $t^*_{ref} = t_{ref}\lambda_L^2$, which results in 31.9 s, i.e., 16 times lower than the reference time in the real SYN cabin (510 s).

After the design and construction of the experimental facility for validation, hot-wire anemometry has been employed to measure the velocity horizontal distribution at the lower gaps of the cabin doors in the small-scale model (the locations with the highest expected velocities to reduce the uncertainty of the experimental data – note also that bulk velocities inside the cabin are excessively low to be measured with the hot wire). A picture of the experimental set-up (note the realistic detail of the lateral grilles manufactured using a 3D printer) with the hot-wire velocimeter is shown in Fig. 7. High precision has been assured with the anemometer, with a frequency response of 1 KHz and acquiring measuring times of 10 s to guarantee signal stability. Hence, only a 0.6% fluctuation of the

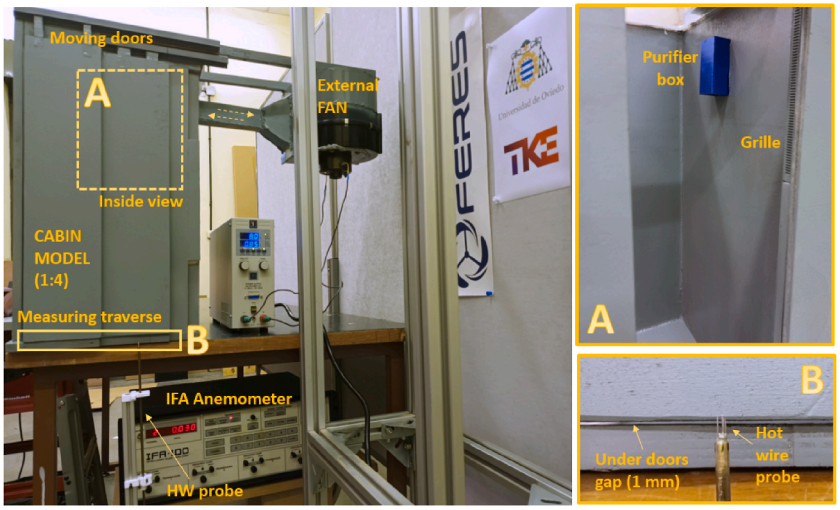

Fig. 7. Experimental set-up designed and constructed for validation.

measured velocities at the required range (0.5–1.0 m/s) has been obtained, with typical uncertainties around 2.5–5% in the velocity magnitude during the probe calibration [43]. The velocities are made non-dimensional with the jet velocity at the purifier outlet to take into account the scaling effects of the similarity. The measured distributions along the doors width are shown in Fig. 8 comparing numerical and experimental results for the most representative cases 1 and 3. A mean absolute percentage deviation of 9.8% and 11.6% has been respectively obtained between numerical and experimental values, which is a reasonable agreement for the validation of the numerical dataset.

2.8.2. Impact of the passenger's volumes

In the present investigation, the impact of the passengers' volume over the global flow recirculation within the cabins has been considered marginal. The average volume of a human body can be assumed to be around 0.08 m^3 (for a typical 80 kg-weight and average density of 1010 kg/m^3 [44]). In the SYN cabin, with a maximum capacity for 4 people, this turns into 0.32 m^3, which represents roughly a 10% of the total volume of the cabin (3.4 m^3). Similar values are obtained if we consider frontal or lateral areas of the human bodies instead of total volume to estimate a cross-sectional blockage (6.5% in the azimuthal direction or 11.7% in the lateral direction). Additionally, for evident comfort considerations, the air purifiers are never blowing directly towards the passengers. Instead, they are located on lateral walls (or in the cabin ceiling) injecting purified air (without age) along the cabin walls, thus allowing a non-obstructed spreading of the jet flow. This also helps to make the blockage of the human bodies over the global flow patterns even less relevant.

Whatever the case, additional simulations including two mannequin bodies in the SYN cabin have been executed for comparison with respect to the original results with the empty cabin. This occupancy rate has been selected because it is one of the most typical situations in the real operation of the cabin (as reported by the manufacturing company). The overset mesh utility of ANSYS Fluent has been employed for a fast construction of the new model. Each mannequin is meshed within an enclosed volume and a 5 mm discretization on the mannequin surfaces with extra refinement in the mannequin boundary layers. Pathlines for cases 1, 3, 5 and 6 of the purifier position have been considered for the comparison (see Fig. 9). The new simulations confirm that the volumetric effect of the bodies is secondary for the establishment of the major recirculation patterns. Note that cases 5 and 6, with the purifier on the ceiling, are particularly unaffected by the inclusion of the bodies. Only in case 1, there is a slight shadow effect of the bodies over some global recirculation in the upper part of the cabin. Hence, the proximity of the bodies head to the suction inlet of the purifier hinders the establishment of a more intense recirculation, though this is clearly dependant on the position of the bodies (in case 3, it is almost marginal).

These visualization results are also confirmed with the direct comparison of the MAA values obtained from SYN cabins with mannequins with respect to those found (see later section 3.2.2) in case of empty cabins, as shown in Table 6:

Firstly, a difference around a 10% (ranging from 7.4 to 18.6%) in the averaged values of the MAA between the empty and occupied cabins is found. This is consistent with the roughly reduction of a 10% in the volume occupied by the air in the cabin (note that the MAA is computed from the accumulative MAA in the fluid cells, with an absent 10% of cells). Secondly, the comparison between the difference scenarios with passengers is also coherent with the general conclusions driven later for the empty cases: the highest MAA values are found for cases 2 and 6, which were already disregarded (also case 3 is to be avoided); while best options are cases 5 and 1 (discussed in section 3.2.2).

Considering this prospective comparison and the fact that (1) the number of simulations and cases combining different positions and number of passengers to be checked is intractable for practical reasons; and (2) the assessment of the purifiers is particularly focused on those idle periods when the cabin is not being used but the purifiers are running (up to 45 min) to purify the inside air, the assumption of empty cabins to perform the numerical study is reasonable.

2.8.3. Impact of the thermal load of the passengers

The passengers are supposed to stay inside the cabins only for a few moments during the elevator movement (let's say around 20–30 s). Despite of that reduced period of time, compared to the operative cycle of the purifiers (45 min), the buoyancy-driven flows generated by the thermal boundary layer around the bodies is rapidly established. In particular, an order of magnitude analysis of the

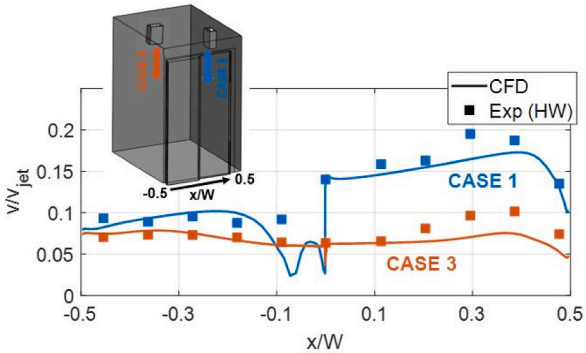

Fig. 8. Comparison of velocity distributions measured and computed at the lower gaps of the cabin for cases 1 (high infiltration) and 3 (low infiltration).

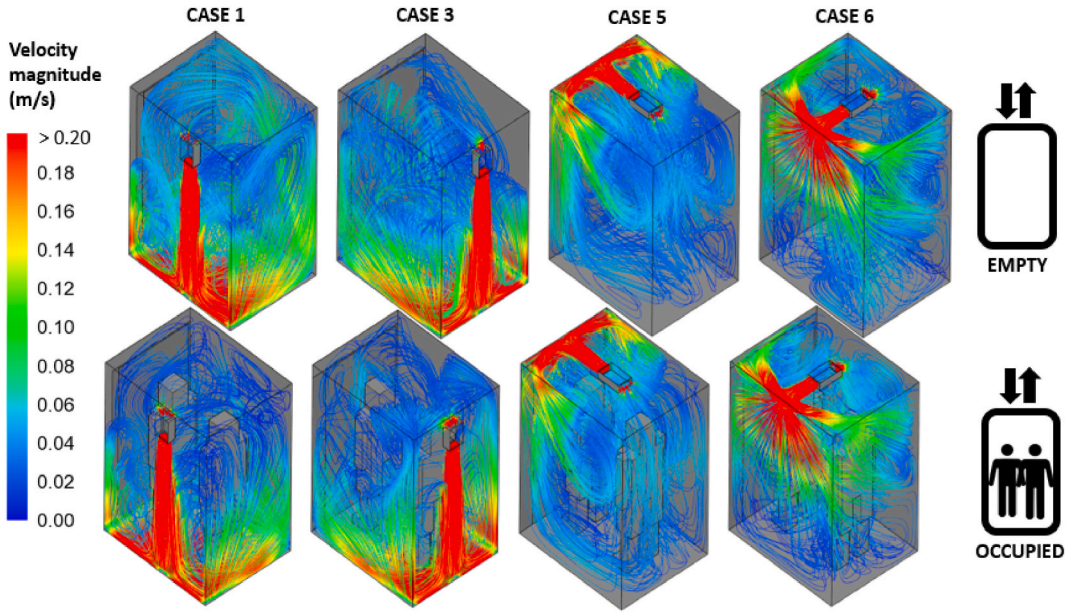

Fig. 9. Comparison of path lines, colored by velocity magnitude, between empty cabin (top) and occupied cabin with two people (bottom).

differential equations gives an estimation of the convective velocities around $u \sim \sqrt{g\beta\Delta TL} \sim 0.6\, m/s$, for a typical metabolic heat generation of 70 W/m^2 in case of a single passenger when standing relaxed. Here, g is the gravity acceleration, β is the thermal expansion coefficient, L a characteristic length (height of the bodies) and ΔT corresponds to the thermal difference associated to the metabolic heat rate. This result leads, in turn, to a boundary layer thickness of $\delta \sim \sqrt{\alpha L/u} \sim 7.5\, mm$ (a few millimetres), where α is the air thermal diffusivity. Finally, the unsteady energy equation for a vertical thermal boundary layer promotes the following time scale for the establishment of the vertical flow currents: $t \sim \delta^2/\nu \sim 2.5\, sec$, where υ stands for the air kinematic viscosity. Effectively, the buoyancy-driven flow is affecting the global flow patterns in the cabin since the very initial moments with relevant velocity values (of the same order than the purifier jetflow). However, note that this is relevant only for the velocity field in the vicinity of the bodies, since the temperature map is practically unaffected. During the total time occupied by the passengers, the global temperature rise produced by the metabolic heat release can be estimated roughly in 1.5 °C for the whole cabin.

To confirm these estimations, and taking advantage of the previous mannequin cases performed for this rebuttal, an additional

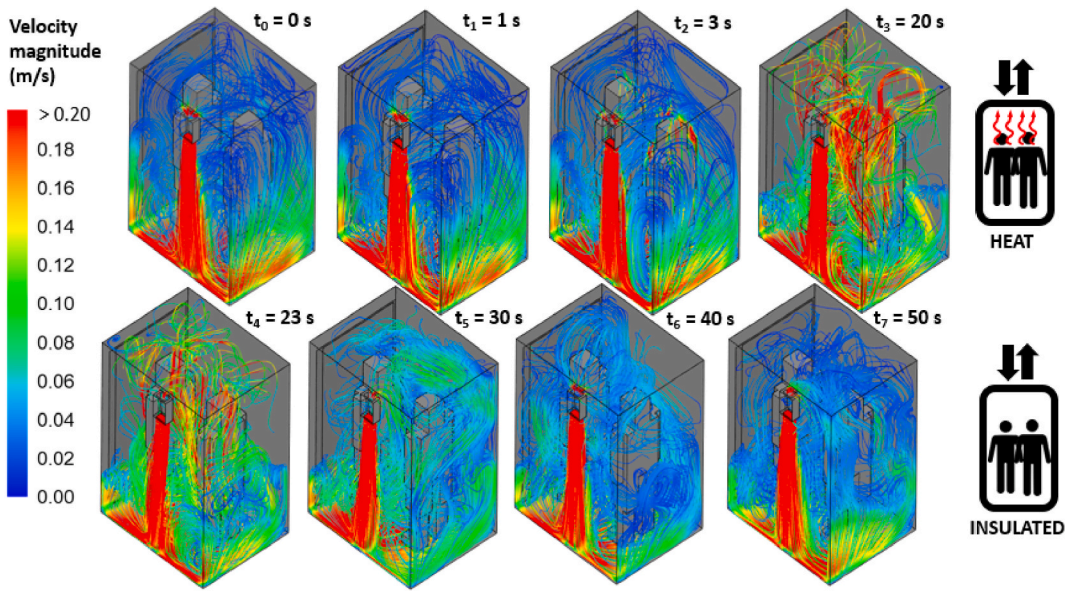

Fig. 10. Evolution of path lines for Case 1. a) Heat input from 0 to 20 s (top); b) Without heat input from 20 to 50 s (bottom).

unsteady simulation has been performed to visualize the thermal plumes generated around the bodies. Hence, a surface heat flux of 70 W/m^2 has been introduced for each mannequin with a characteristic time step size of 0.05 s to resolve the transient evolution of the flow in the cabin. Case 1 with the purifier placed at the middle of the lateral sidewall has been considered. Firstly, an initial stage for 20 s has been computed, checking the flow patterns after 1, 3 and 20 s. Following, and assuming that the passengers have already abandoned the cabin so no more heat flux is released inside, a second stage without thermal input was resolved for 30 additional seconds. Impact of the thermal buoyancy is then clearly shown in Fig. 10. After 1 s, the thermal boundary layer is still not developed. However, as predicted by the inspectional analysis, significant vertical currents (>0.2 m/s) are induced around the bodies after 3 s (although the initial global flow pattern is still preserved). Definitively, after 20 s, the global pattern is already changed by the buoyancy-driven problem in the central part of the cabin, enhancing the overall mixing, completely modifying the original recirculation and thus accelerating the air renewal. When the thermal input stops (bottom row, modelled as insulated bodies), the agitation is rapidly decayed and the original pattern due to the mechanical-driven flow of the purifier is progressively restored. Effectively, at 23 s, the thermal plume is quite weakened, while at 30 s is completely vanished. After 40 s, the resemblance of the present pathlines with the originals is clear, and at 50 s, the final distribution is almost identical to the initial patterns.

Obviously, this confirms the relevance of the thermal effects, but reveals how these mechanisms are instantaneously triggered and disabled. As expected, the simulation demonstrates that they are no longer affecting the flow after 50 s, when the passengers have already left the cabin. Considering that the typical reference renewal time of the cabin is 510 s (with mean ages of air of the same order), this means that only a 10% of the cycle is conditioned by the thermal problem.

In summary, despite of this significant restriction, the present set of non-thermal simulations is considered to be more representative and useful for the real goal of our research: the assessment of the purifiers focused on idle periods when the cabin is not being used by passengers, but the purifiers are running (up to 45 min) to purify the inside air, justifying the simplifications adopted.

2.9. Air Change Effectiveness (ACE)

To evaluate the ventilation effectiveness, an additional metric proposed in the literature [30] and known as "Air Change Effectiveness" (ACE) was used. It is defined as the ratio between the values of mean age of air (MAA) for a given region, and the reference time (T_{ref}) corresponding to the quotient between the cabin volume (V_{Cab}) and the purifier flow rate (Q_0):

$$T_{ref} = \frac{V_{cab}}{Q_0} \tag{8}$$

$$ACE = \frac{T_{ref}}{MAA} \tag{9}$$

The reference times for both EVO and SYN cabins are 740 and 510 s respectively (Table 4).

In this work, the ACE values have been obtained in three different zones:

- Local ACE: computed from the mean age of air in the aspirating section of the air purifier (cabin domain outlet).
- Global ACE: computed from the volume-averaged value of the mean age of air in the whole cabin domain.
- Occ. ACE: computed from the volume-averaged value of the mean age of air in the occupied volume (associated to an averaged range of heights for the passengers' heads, between 1.45 and 1.75 m).

As a reference, the literature refers to the unity as the threshold limit between the different ventilation modes. Thus, ACE values less than 1 indicate poor ventilation caused by short circuits and stagnation zones; values close to 1 indicate perfect mixing of the purified air with the "old" air and values greater than 1 indicate piston-type ventilation. The latter is the ideal situation for the cabin ventilation, in which the purified air displaces the "old" air with almost no mixing, hence reducing possible exposure times.

3. Results

3.1. EVO cabin

3.1.1. Global flow patterns and infiltration flow rates

Firstly, the infiltration flow rates of the six cases studied for the EVO cabin have been analyzed (Table 7). It is observed that, depending on the position of the purifier, there is a notable difference in the distribution of infiltrations. In general, the infiltrations are greater in the gaps than in the grilles, due to the significant restrictions imposed by the grilles louvres. This indicates the need for a good estimation of the loss coefficients in the grilles, as well as a good modelling of all the clearances and gaps, critical for the accurate estimation of all the infiltrations. It is relevant the high infiltration levels achieved in the most favorable cases. The positions that

Table 7
Infiltration rates in the EVO cabin for the different positions of the purifier.

Q (m^3/h)	C1	C2	C3	C4	C5	C6
Example gap (under doors)	−2.174	−1.243	−0.314	−0.457	0.747	−0.156
Example grille (back corner grilles)	0.132	−0.540	−0.464	−0.604	−0.545	0.975
Infiltration flow rate	3.507	2.258	1.236	1.642	3.975	2.978
Relative infiltration flow rate [%]	9.61	6.19	3.39	4.5	10.89	8.16

provide a higher infiltration rate (around 10% of the mechanical flow rate) are 1 and 5, while cases 3 and 4 are found to provide the lower ones (around 4%).

Fig. 11 illustrates the comparison between case 1 (high infiltration rate) and case 3 (lowest infiltration). The velocity field in all the slots and gaps is represented with scaled vectors, which have been colored by the velocity magnitude. In case 1, most of the outgoing flow escapes through the floor gap under the doors, while the rest goes out through the lower area of the gaps between the doors, as well as through the corner gaps and side and top louvers. On the contrary, most of the incoming flow is found in the middle and upper zones of the gaps between doors (with a maximum infiltration value in that zone of -2.17 m^3/h, see Table 7), as well as the ceiling gap of the doors and the corner grilles. On the other hand, in case 3, the highest outgoing flows correspond to the corner grilles area (value -0.46 m^3/h in Table 7) and also to the floor gap under the doors, while the largest source of incoming flow is observed in the circular grilles of the ceiling.

Since the infiltration regions are generally concentrated in the door zone, the proximity of the air purifier to the cabin doors appears to be a significant factor to enhance the infiltrations. In particular, the notable differences in the intensity of the velocity vectors between case 1 and 3 shown in Fig. 11 support this hypothesis.

Following, the velocity distribution in a horizontal plane of the cabin, 1.6 m high from the floor, is shown in Fig. 12 for cases 1, 3 and 6. This plane has been taken as a reference for the typical height of the passengers' heads. For a better representation, these velocity maps have been limited to a maximum value of 0.2 m/s. The high velocity spots, corresponding to the jet core released from the air purifiers, are located on the sidewalls of cases 1 and 3. For case 6, the high velocity region, found in the right lateral wall, is a consequence of the downward change of direction of the initial horizontal jet (after impinging the sidewall). In addition, moderate-to-low velocity regions (yellow and green zones) present some symmetries for the cases located in the walls. Likewise, the bulk flow is concentrated in the corners and lateral sides, as a consequence of an upwards recirculation of the air coming from the floor.

3.1.2. Mean age of air distributions

Mean ages of air (MAA), computed from different zones of the EVO cabin, have been obtained for all the positions analyzed for the air purifier (Table 8). Overall vales for the cabin area are found to be between 500 s and 540 s. Moreover, when the MAA at the outlet is lower than the volume-averaged value in the cabin, short circuits and dead volumes are expected to be found in those cases. Precisely, cases 2 and 6 present this detrimental characteristic. On the other hand, a direct comparison of the values obtained in the occupancy volume with those obtained for the rest of the cabin also allows to identify the best-ventilated regions in each case. For example, cases 3 and 4 have a cabin MAA significantly lower than that of the occupancy volume, indicating its superior performance to ventilate the lower zones of the elevator, while case 6 presents an opposite trend. Note that case 1 provides the lowest air age in all the zones.

Fig. 13 shows a 3D representation with contours of mean age of air in the EVO cabin, comparing the best case (1) with the worst case (6). Note that this type of representation is a good tool to visualize how the cabin ventilation is performing.

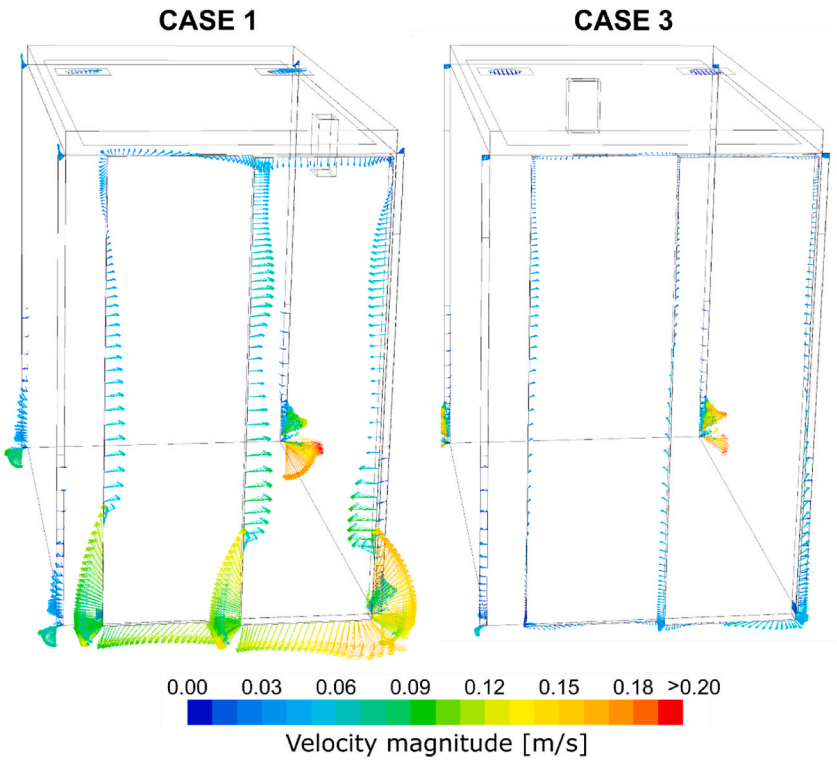

Fig. 11. Velocity vectors in the infiltration zones of the EVO cabin (colored by velocity magnitude. A) Case 1 (high infiltration rate). B) Case 3 (low infiltration rate).

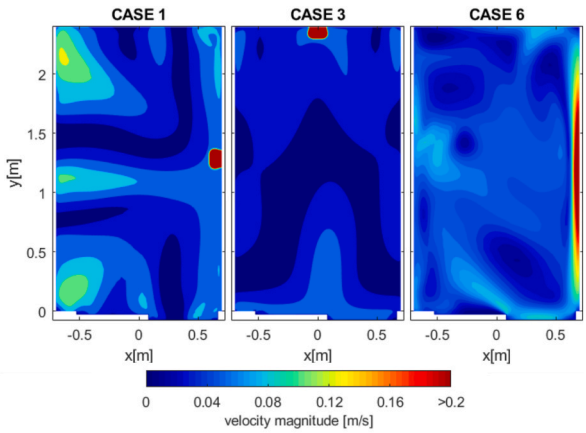

Fig. 12. Velocity distributions in the EVO cabin at 1.6 m high.

Table 8
Mean ages of air in the EVO cabin for the six different positions of the purifier.

	MAA [s]					
Zone	C1	C2	C3	C4	C5	C6
Outlet	517	524	546	539	527	532
Cabin	501	531	505	505	510	536
Occupied zone	505	530	521	522	517	507

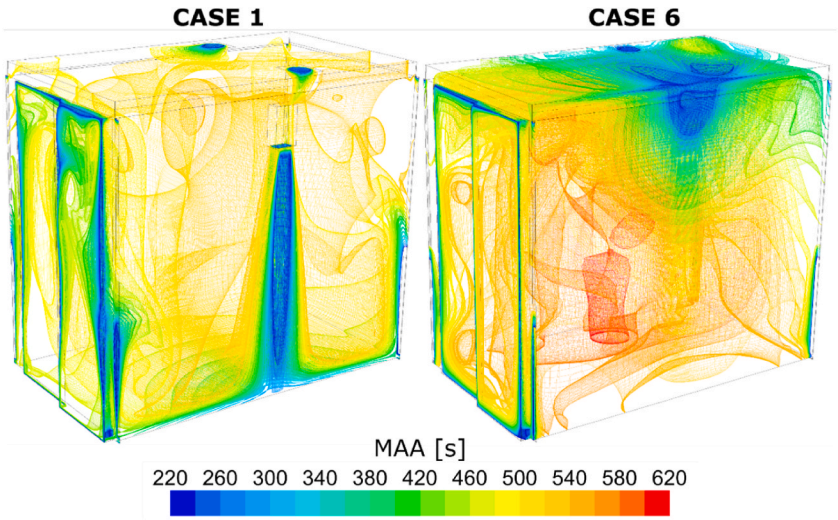

Fig. 13. 3D representation (contours) of the MAA inside the EVO cabin for both best (case 1) and worst (case 6) ventilation scenarios.

It is revealed that case 1 makes better use of the natural infiltration elements (louvers and gaps), especially in the door area (more intense blue zones than case 6). In addition, a significant homogeneous ventilation can be observed for the entire volume of the cabin. On the other hand, case 6 presents a very unbalanced ventilation, with higher MAAs in general, and where dead volumes can be even identified in the bottom central area of the cabin.

Concerning the most critical area (the occupancy volume for the users), contours of MAA have been plotted on the horizontal plane at a height of 1.6 m (Fig. 14). Once more, the position of the air purifier is well identified by the darker blue areas. In cases 1 to 4, that blue spot corresponds to the core jet coming from the purifier located on the sidewalls. For cases 5 and 6, the blue region is associated to the recirculated air currents going downwards after impinging the lateral walls (at $y = 0$ for case 5 and $x = 0.7$ for case 6). The other small dark blue spots correspond to the infiltration zones which are contributing marginally to the air renewal. Precisely, these localized zones are not able to have a significant impact on the overall pattern of the cabin. However, it is also observed that they can better contribute if they are properly reinforced by the jet core circulation. As shown previously, case 6 shows a very unbalanced

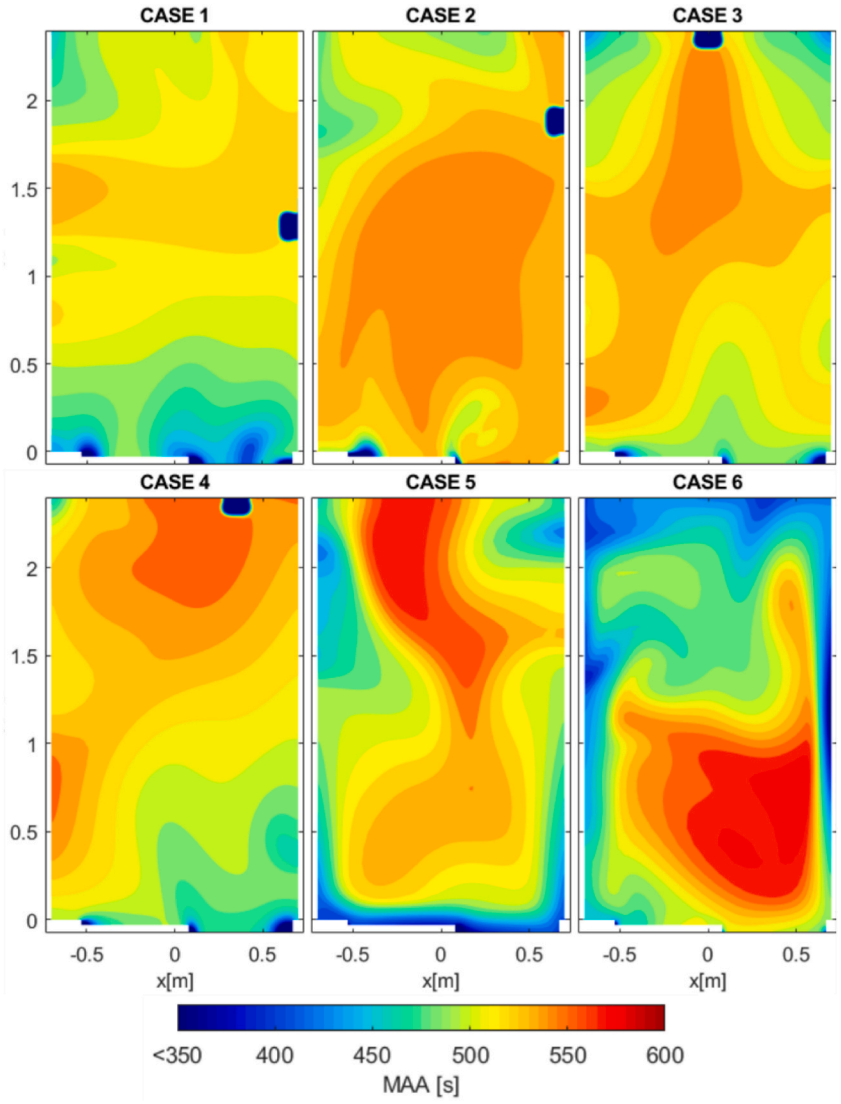

Fig. 14. Contours of MAA at the 1.6 m high horizontal plane for all the air purifier positions in the EVO cabin.

distribution of MAA in the cabin, presenting two distinct zones. Case 2, and even cases 3 and 4, also produce deficient distributions of MAA. Conversely, cases 1 and 5 demonstrate their better ability to promote an efficient air renewal, although case 5 is notably less homogeneous.

3.1.3. Air change effectiveness

ACE values obtained for the different cabin zones in all the cases studied for the EVO cabin are shown in Table 9. All cases present ACE values higher than one in all the zones analyzed. Generally speaking, this reveals that all the positions studied are able to provide a good air renewal. This conclusion is even valid for cases 2 and 6, which seemed to be bad candidates according only to their flow patterns. Consequently, it can be affirmed that the performance of the air purifier is well matched to this type of cabin. In any case, a

Table 9
ACE values in the EVO cabin for the six different positions of the purifier.

	ACE [−]					
Zone	C1	C2	C3	C4	C5	C6
Local	1.43	1.41	1.36	1.37	1.41	1.39
Global	1.48	1.39	1.46	1.47	1.45	1.38
Occ.	1.47	1.40	1.42	1.42	1.43	1.46

comprehensive analysis of all these results points out that the most recommendable positions for the purifier in the EVO cabin are: firstly, and significantly better than the others, the position centered on the sidewall (case 1) and secondly, as an alternative position, in the cabin roof, centered and blowing towards the door (case 5).

3.1.4. Blowing direction

Once the best positions have been identified, an additional set of simulations are performed to check the influence of the blowing direction on the overall ventilation. Therefore, two new situations are executed for cases 1 and 5, but swapping inlet and outlet conditions for the air purifier. These inverted cases imply blowing upwards to the ceiling (case 1inv) and blowing horizontally towards the cabin backside (case 5inv).

Firstly, the flow patterns in the cabin are analyzed for these new scenarios. For that purpose, streamlines have been drawn from both the inlet (suction) and outlet (discharge) boundaries of the purifier and colored with the values of the mean age of air (Figs. 15 and 16). This representation allows the identification of the air paths throughout the cabin and its progressive aging.

The comparison between case 5 and case 5inv can be seen in Fig. 15. In the conventional case 5, the air discharged by the purifier impinges the upper zone of the doors where it finds a corner step that acts as a deflector. As a consequence, part of the flow is diverted towards the center of the cabin while the rest is distributed towards the floor and along the side walls. All the flow is then progressively driven to the opposite side of the cabin where it is suctioned towards the purifier inlet. On the other hand, in the inverted case, the jet impacts onto the backside wall, bouncing back and returning to the purifier inlet without being sufficiently distributed throughout the whole cabin. Thus, the lack of that deflecting geometry involves a very local evolution that prevents a correct ventilation. A large region in the bottom part of the cabin is then recirculated, with the air progressively aging and leading to high MAA values.

Similar representations have been obtained in Fig. 16 for cases 1 and 1 inverted. In the conventional case 1, it can be clearly seen how the jet core hits the floor and is distributed throughout the cabin following the sidewalls and doors, being more concentrated in the corners. In the doors area, this recirculating pattern allows the reinforcement of the infiltration rates through gaps and slots. In the upper region of the cabin, part of the air is captured by the purifier suction, while the remaining air goes towards the central zone generating two large vortices. Note also a large portion of suctioned air coming from the left corner of the backside wall in the cabin, where higher values of MAA are found.

Meanwhile, in case 1 inverted, the jet splits immediately after impinging onto the ceiling. On the one hand, two jets are generated, bouncing back at both sides of the purifier, and redirected downwards to the central region of the cabin. On the other hand, the rest of the jet enters into the false ceiling, enabling its further distribution throughout the rest of the cabin. Basically, the upper zone receives renewed air from both sides of the false ceiling, with the two jets displacing the rest of the air; while the inlet of the purifier aspirates air from the central zone of the volume where the air is more aged.

Finally, in order to have a quantitative indicator, the levels of ACE in all the relevant zones of the cabin were compared for both conventional and inverted cases. The results are shown in Table 10. ACE values for case 5inv are particularly poor, due to the low levels of Global and Occ. ACE, which indicate the existence of short circuits and dead volumes in the cabin. On the contrary, case 1inv reveals a slight improvement with respect conventional case 1 in all the indicators. However, considering the comparison of MAA patterns in the plane at 1.6 m high (Fig. 17), it can be observed that the air concentrated in the central area (most likely to be occupied) is the one with the highest mean age for the inverted case. Moreover, since the false ceiling is the geometrical characteristic that it is conditioning the flow patterns of the inverted case, and considering its simplified modelling (without luminaires, wiring, folds, supports, etc.), real conditions for this element could obstruct the flow, making the purifier less efficient than the conventional case 1.

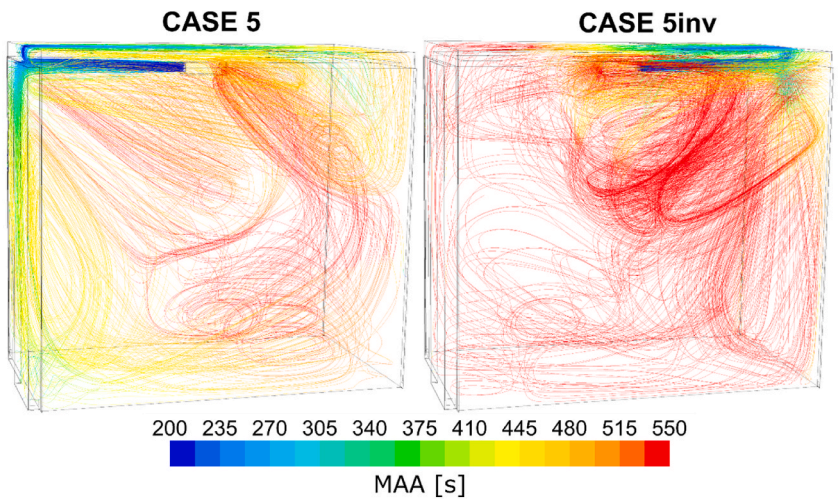

Fig. 15. Comparison of flow streamlines (colored by MAA values) in the EVO cabin for cases 5 (left) and 5 inverted (right).

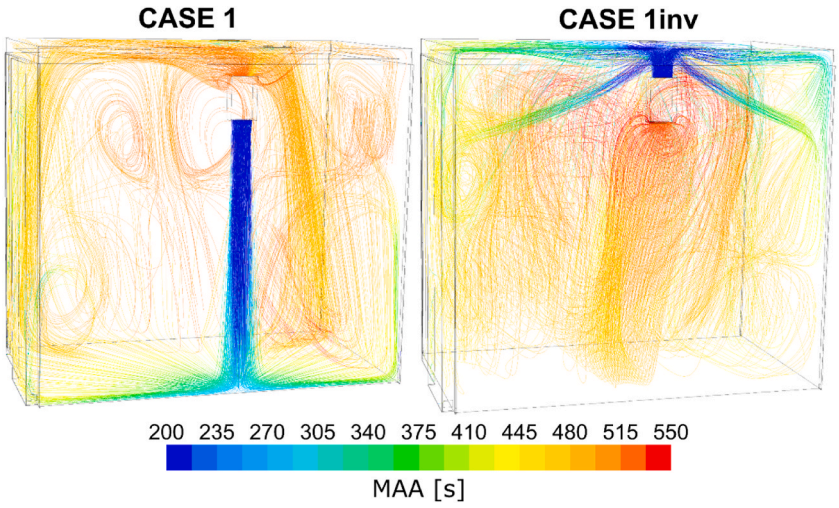

Fig. 16. Comparison of flow streamlines (colored by MAA values) in the EVO cabin for cases 1 (left) and 1 inverted (right).

Table 10
ACE values in the EVO cabin for the best positions of the purifier and comparison with their corresponding inverted cases.

	ACE [−]			
Zone	C1	C1-inv	C5	C5-inv
Local	1.43	1.38	1.41	1.37
Occ.	1.47	1.5	1.43	1.16
Global	1.48	1.55	1.45	1.14

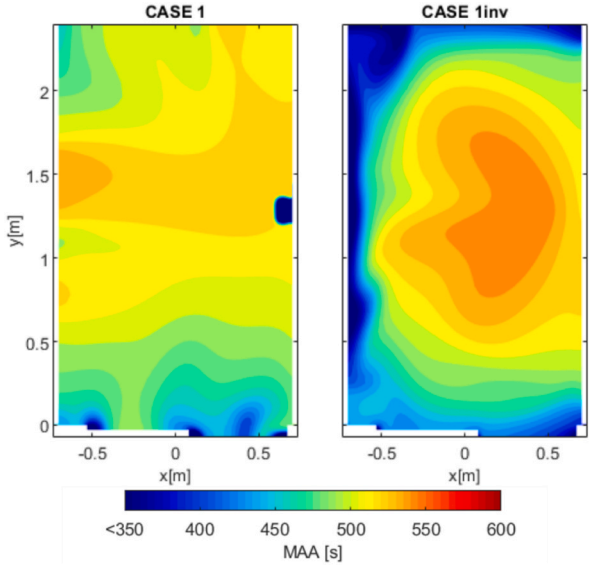

Fig. 17. Comparison of MAA contours at the 1.6 m high horizontal plane for cases 1 and 1 inverted in the EVO cabin.

3.2. SYN cabin

3.2.1. Global flow patterns and infiltration flow rates

The SYN cabin has a simpler geometry than the EVO, with fewer but larger infiltration zones. Complementarily, due to its lower volume, the design flow rate for the purifier is reduced leading to smaller infiltration rates than in the EVO cabin. Despite of this downscaling, the overall trends are similar in the SYN cabin, so cases 1 and 5 induce again the highest values of infiltration. Comparing the relative flow rates of both cabins, it is observed a reduction in the flow rate for the sidewall cases (1 and 2) in this cabin, probably

due to the absence of grilles and slots in the corners. On the contrary, the infiltration for the backwall cases (3 and 4) increases in relative terms. This increase is easily attributable to the smaller length of the cabin, and the consequent shorter distance from the purifier to the door area. Considering the cases with the purifier on the ceiling, the relative infiltration for case 5 is increased, due to the upper zone louvers in the inlet frame, while for case 6 decreases, perhaps due to the absence of ceiling louvers and corner gaps.

The velocities in the infiltration zones for cases 1 and 3 are compared in Fig. 18. Although there is still a difference in magnitude between the two cases, it has been now significantly reduced for the SYN cabin. Moreover, the behavior of both cases is much more similar than in the EVO cabin, presenting the same inflow and outflow zones. Only the lower zone of doors gap, the upper right zone of the door-elevator gap and the upper right grille (-0.203 m^3/h compared to 0.014 m^3/h in Table 11) present slight differences.

Fig. 19 shows the velocity distributions in the horizontal plane at 1.6 m high of the SYN cabin. In case 1, the distribution of the ascending air currents (in the left sidewall) changes with respect to the same case of the EVO geometry, presenting two zones (instead of three) and with their position shifted from the corners and center to intermediate locations. The symmetry of the pattern is also more distorted in the SYN case. Conversely, cases 3 and 6 have distributions more similar to those observed in the EVO cabin, with special homogeneity in case 6 of this cabin.

3.2.2. *Mean age of air distribution*

Mean ages of air (MAA), computed from different zones of the SYN cabin, are now presented for all the positions simulated in Table 12. Typical values of MAA obtained in this cabin, between 335 and 404 s, are lower than those found in the EVO cabin. The lower flow rate of the purifier does not fully compensate the volume reduction of this cabin, thus leading to ages of air significantly lower. In other words, the significant reduction of the cabin volume makes the ventilation easier. Once again, case 6 has lower MAA values at the outlet than inside the cabin, indicating the existence of dead volumes and/or internal short circuits. In addition, the MAA values in the cabin for that case 6 are notably higher than other cases. The best options are again associated to cases 1 and 5, being case 5 the most promising with the lowest MAA. Comparatively, cases 3 and 4 improve their results, in relative terms in the occupancy volume, with respect to the EVO cabin values.

Now, three-dimensional contours of MAA have been represented for cases 1 and 6 in the SYN cabin (Fig. 20).

The figure reveals that the infiltration zones in case 1 are less active than those in the corresponding case for the EVO cabin (Fig. 13). Nevertheless, the overall ventilation and air renewal is still quite homogeneous. On the contrary, in case 6 of the SYN cabin (right image), the lower zones have very high MAA values and ventilation is only efficient in the upper region. This is also consistent with the local sources of infiltration, excessively marginal to modify the overall pattern of ventilation.

This section is concluded with Fig. 21, showing MAA distributions in the horizontal plane at 1.6 m high for all the 6 cases studied in the SYN cabin. These maps are consistent with previous results from the EVO cabin. Hence, case 6 presents ages of air notably higher than other cases, especially in the central zone due to a large dead volume. Likewise, cases 2 and 3 present an unbalanced distribution in the plane, where lower ages are found near the doors and higher values are accumulated in the backside wall. Besides, case 5 has the best distribution in this plane, followed by cases 1 and 4. The infiltration zones provide a larger area of influence than in the EVO cabin, mainly due to the difference in size of the cabins.

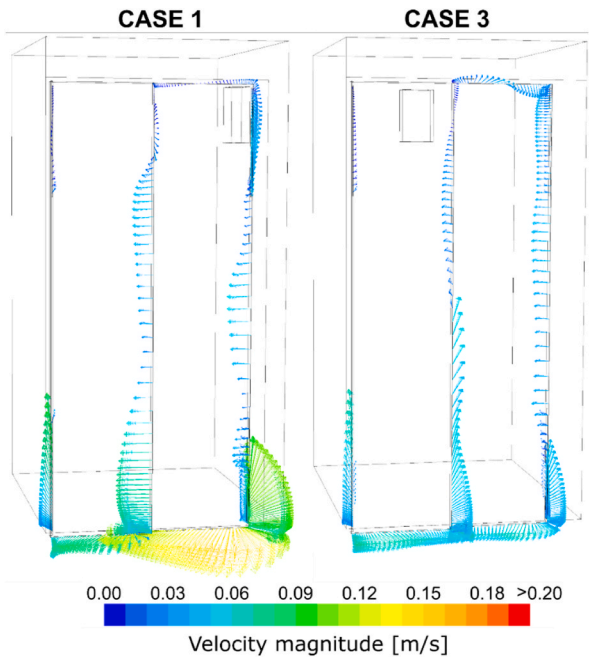

Fig. 18. Velocity vectors in the infiltration zones of the SYN cabin (colored by velocity magnitude. A) Case 1 (high infiltration rate). B) Case 3 (low infiltration rate).

Table 11
Infiltration rates in the SYN cabin for the different positions of the purifier.

Q (m^3/h)	C1	C2	C3	C4	C5	C6
Example gap (under doors)	−0.989	−0.713	−0.850	−0.665	0.049	0.731
Example grille (top grille right)	−0.203	−0.419	0.014	0.542	0.328	−1.769
Infiltration flow rate	1.927	1.402	1.508	1.412	2.684	1.403
Relative infiltration flow rate [%]	8.03	5.84	6.28	5.88	11.18	5.85

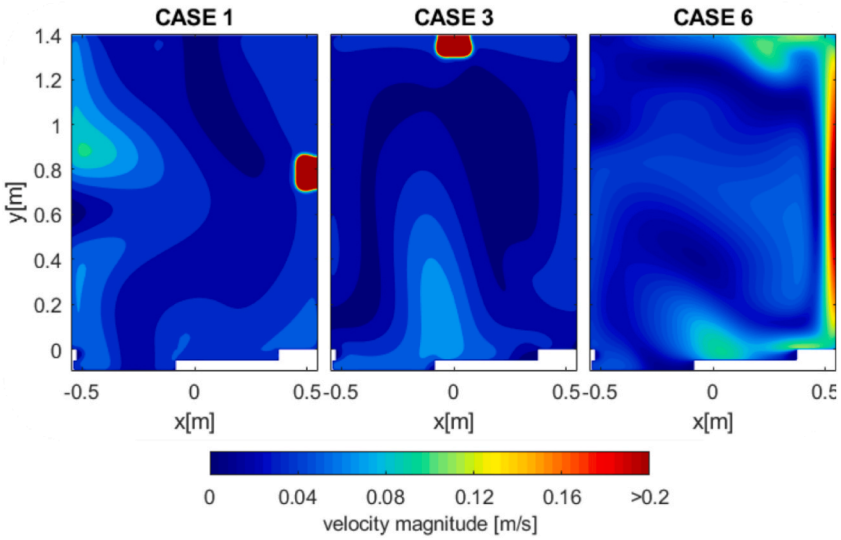

Fig. 19. Velocity distributions in the SYN cabin at 1.6 m high.

Table 12
Mean ages of air in the SYN cabin for the six different positions of the purifier.

	MAA [s]					
Zone	C1	C2	C3	C4	C5	C6
Outlet	372	380	382	383	369	377
Cabin	350	363	352	353	335	404
Occupied zone	360	376	364	358	341	379

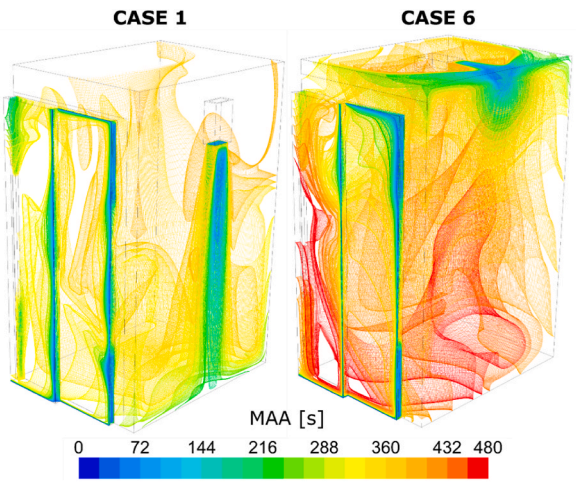

Fig. 20. 3D representation (contours) of the MAA inside the SYN cabin for both best (case 1) and worst (case 6) ventilation scenarios.

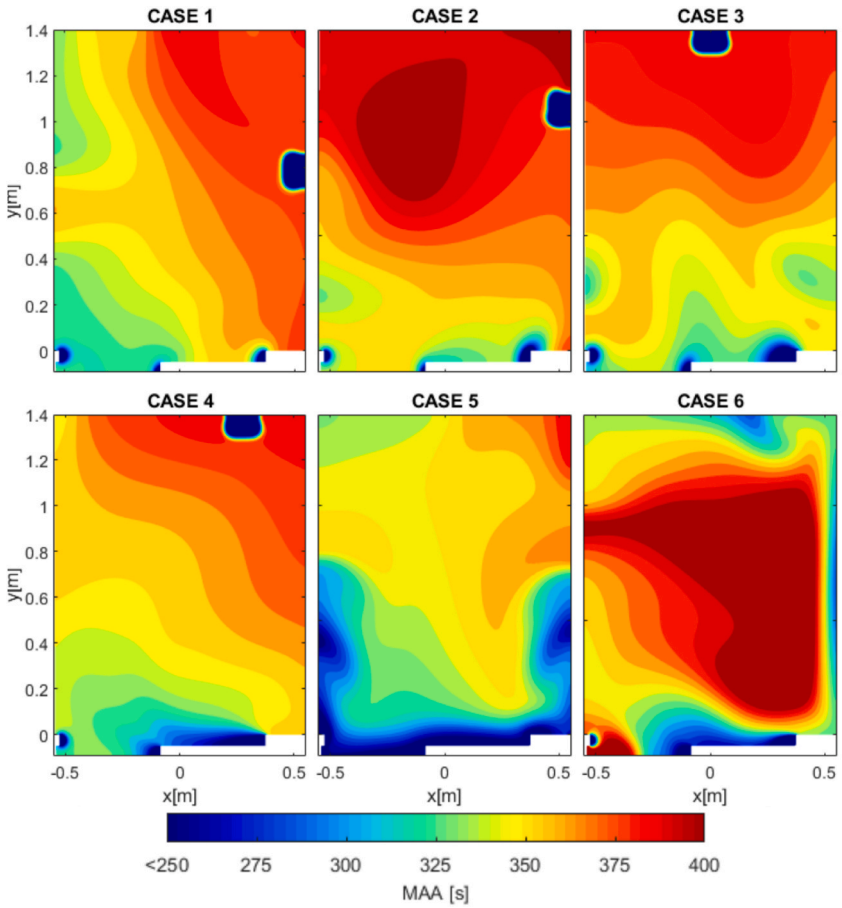

Fig. 21. Contours of MAA at the 1.6 m high horizontal plane for all the air purifier positions in the SYN cabin.

3.2.3. *Air change effectiveness*

ACE values, as a function of the cabin zone in the different cases for the SYN cabin, are shown in Table 13. Once again, it is revealed that the performance of the air purifier is well matched to this type of cabin, presenting ACE values higher than one for all the scenarios. The best results (highest ACE) correspond to cases 1 and 5, while the worst option is given by case 6.

3.2.4. *Blowing direction*

Finally, the influence of the blowing direction has been also studied for the SYN cabin. In particular, only the inverted case 1 (Case 1inv) was studied. Case 5 inverted was not considered due to poor results observed for the EVO cabin (worse results that any other case) and the presumable similarity expected now for the SYN cabin (note the overall similar results obtained for both cabins in previous sections).

Firstly, the basic flow patterns in the cabin are analyzed with the same previous methodology. Fig. 22 shows the results for cases 1, 1 inverted and 5.

The flow patterns in these three cases of the SYN cabin are very similar to those presented earlier for the EVO cabin. It is worth highlighting inverted case 1, which is more interesting now because of the absence of a false ceiling. This implies that the results become more representative of the ceiling region. In particular, with the air purifier installed close to the ceiling, the jet core is roughly mixed out, without suffering significant diffusion (unlike conventional case 1, where the jet widens as goes downward reducing its bulk velocity) and conserving its momentum after impinging the ceiling. As a consequence, the roof itself diverts the air flows towards the

Table 13
ACE values in the SYN cabin for the six different positions of the purifier.

	ACE [−]					
Zone	C1	C2	C3	C4	C5	C6
Local	1.37	1.34	1.34	1.33	1.38	1.35
Global	1.46	1.41	1.45	1.45	1.52	1.26
Occ.	1.42	1.36	1.40	1.42	1.50	1.34

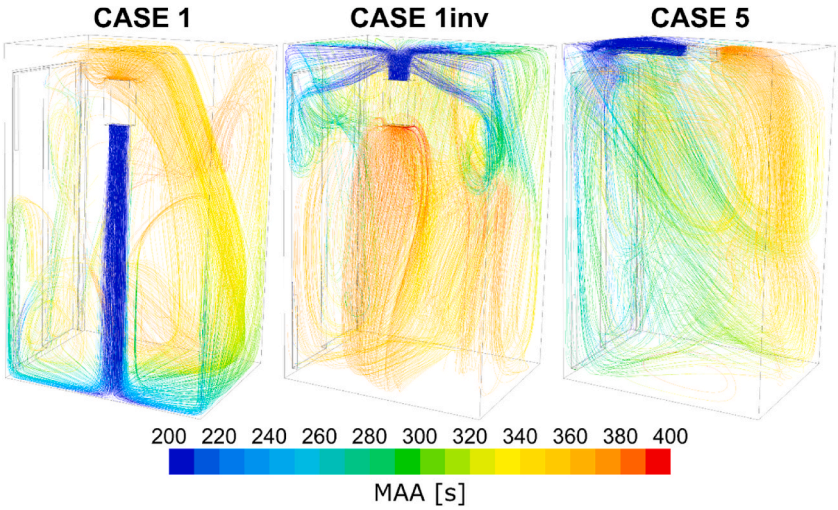

Fig. 22. Comparison of flow streamlines (colored by MAA values) in the SYN cabin for cases 1 (left), 1 inverted (middle) and 5 (right).

lateral sides, but also downwards with two bouncing jets. Moreover, as the jet preserves its momentum, the major part of the flow is distributed from the ceiling; not only going downwards onto the lateral sides, but also going into the center of the cabin. Finally, the suction contributes to the movement of air from the lower zone. This means that the aspirating region is contributing to a more intense air movement in the lower zone.

In addition, Fig. 22 shows how both inverted case 1 (middle) and case 5 (right) are very likely to interact negatively with the opening of doors, so this aspect should be studied in greater depth for a future work.

To conclude, the ACE levels of these three cases are shown in Table 14. Notice that case 1 inverted represents a slight improvement over conventional case 1 (for the ACE Global level), and a notable improvement, especially in the occupancy volume where it even improves case 5, the option with best results so far.

4. Conclusions

The optimal position of an air purifier for elevator cabins has been determined, in terms of ventilation and air renewal, using advanced CFD techniques in a full 3D unsteady numerical model. The assessment of the purifiers has been mainly focused on idle periods when the cabin is not being used by the passengers but the purifiers are still running during 45 min to avoid that the trapped air in the cabin could suppose a reservoir for contaminants.

Neither the volume occupied by the passengers, nor the heat transfer released to the ambient has been considered in the study. These modelling restrictions have been addressed carefully with additional simulations demonstrating that they can be reasonably neglected for the objectives of the study. The results of preliminary simulations including the volumetric blockage of the passengers' bodies are consistent with the major findings observed for empty cabins. Also, since thermal effects contribute to enhance the flow mixing and reduce the MAA (preventing dead volumes), its absence leads to more conservative scenarios, with a major challenge for the ventilation effectiveness.

A 3D resolution of the unsteady RANS equations for the air flows using a k-ε RNG turbulence model, has provided a validated estimation of MAA distributions inside the cabins, revealing that the contribution of infiltrations is significant for the global results, with values of up to 10% of total recirculated flowrate of the purifier.

Regarding the results, six different locations for two different cabin geometries were studied. It has been found that the flow patterns induced by the air purifier are similar for both cabins, so the conclusions of the present study can be generalized to other cabins. Infiltration zones contribute to a better ventilation, but with less influence on the evolution of the overall pattern than expected. The enhancement of the flow exchange in these zones is very positive for ventilation, so the proximity of the purifier to the infiltration zones can be concluded as a relevant factor. In both cabins studied, cases 1 and 5 are identified as the best positions to maximize the air renewal, blowing downwards to the cabin floor and towards the cabin doors respectively.

Table 14
ACE values in the SYN cabin for the best positions of the purifier and comparison with their corresponding inverted cases.

	ACE [−]		
Zone	C1	C1-inv	C5
Local	1.37	1.32	1.38
Global	1.46	1.48	1.52
Occ.	1.42	1.52	1.50

The cases studied with the inverted blowing direction (EVO-C5inv, EVO-C1inv and SYN-C1inv) are only positive in case of position 1, mainly due to the closer proximity of the purifier to the ceiling (instead of the floor) and a superior conservation of the jet core momentum. In addition, it has been observed that when the jet impinges onto some irregular geometry better results are achieved. This indicates that the inclusion of diffusers or some type of deflector geometries at the outlet of the purifier could be beneficial for improving its performance.

Finally, it must be advised that these global conclusions for the scenarios studied are likely to be significantly influenced by the effect of the doors opening and closing in a typical cycle time of the elevator. This aspect, which is beyond the scope of this paper, is proposed for future work in order to provide a more comprehensive picture of the ventilation and air renewal in this type of elevator cabins using air purifiers.

Authorship statement

All persons who meet authorship criteria are listed as authors, and all authors certify that they have participated sufficiently in the work to take public responsibility for the content, including participation in the concept, design, analysis, writing or revision of the manuscript.

Furthermore, each author certifies that this material or similar material has not been and will not be submitted to or published in any other publication before its appearance in the Journal of Building Engineering.

List of all authors:

- Santamaría Bertolin, Luis (University of Oviedo).
- Fernández Oro, Jesús Manuel (University of Oviedo).
- Argüelles Díaz, Katia María (University of Oviedo).
- Galdo Vega, Mónica (University of Oviedo).
- Velarde-Suárez, Sandra (University of Oviedo).
- Fernández, Luis Joaquín (TKE Elevator Innovation Center).
- Del Valle, María Elena (TKE Elevator Innovation Center).

Declaration of competing interest

The authors declare that they have no known competing financial interests or personal relationships that could have appeared to influence the work reported in this paper.

Data availability

Data will be made available on request.

Acknowledgements

The authors would like to thank the financial support provided by the CDTI, "*Centro Tecnológico para el Desarrollo Industrial*" from the Spanish Ministry of Science and Innovation, under the National Strategic Program CIEN, for the granting of the project "INN-MEDICAL: Innovative Medical Industry enabling an Efficient and Autonomous Response against COVID-like Pandemic". Also the technical support given by the staff of the TK Elevator Innovation Center, within the framework of the contract CN-21-032-CDTI at the University of Oviedo, for the development of the study "Optimal Position of the Air Novum device in elevator cabins" is gratefully acknowledged.

References

[1] L. Morawska, J.W. Tang, W. Bahnfleth, P.M. Bluyssen, A. Boerstra, G. Buonanno, C. Haworth, How can airborne transmission of COVID-19 indoors be minimized? Environ. Int. 142 (2020), 105832.
[2] G. Buonanno, L. Stabile, L. Morawska, Estimation of Airborne Viral Emission: Quanta Emission Rate of SARS-CoV-2 for Infection Risk Assessment, Environment International, 2020, 105794.
[3] Y. Li, H. Qian, J. Hang, X. Chen, P. Cheng, H. Ling, M. Kang, Probable airborne transmission of SARS-CoV-2 in a poorly ventilated restaurant, Build. Environ. 196 (2021), 107788.
[4] T. Dbouk, D. Drikakis, On airborne virus transmission in elevators and confined spaces, Phys. Fluids 33 (2021), 011905.
[5] Sumei Liu, Xingwang Zhao, Stephen R. Nichols, Murilo W. Bonilha, Tricia Derwinski, James T. Auxier, Qingyan Chen, Evaluation of airborne particle exposure for riding elevators, Build, Build. Environ. 207 (2022) 108543.
[6] Nirvik Sen, Transmission and evaporation of cough droplets in an elevator: numerical simulations of some possible scenarios, Phys. Fluids 33 (2021), 033311.
[7] S. Nichols, J. Auxier, Airflow and Elevators: Highlights of an Airflow Study Conducted to Determine the Relative Risk of COVID-19 Transmission Among Elevator Passengers, Otis Elevator Company, Communication, 2021. January 2021.
[8] Q. Chen, S.L. Zhao, S. Liu, Evaluation of COVID-19 Infection Risk when Taking Elevators, Otis Elevator Company communication, 2020. December 2020.
[9] Talib Dbouk, Frederic Roger, Dimitris Drikakis, Reducing indoor virus transmission using air purifiers, Phys. Fluids 33 (10) (2021), 103301.
[10] N.N. Peng, H.W. Chow, C.H. Liu, Computational study on the transmission of the SARS-CoV-2 virus through aerosol in an elevator cabin: effect of the ventilation system, Phys. Fluids 33 (10) (2021), 103325.
[11] M. Hagbom, J. Nordgren, R. Nybom, K.O. Hedlund, H. Wigzell, L. Svensson, Ionizing air affects influenza virus infectivity and prevents airborne-transmission, Sci. Rep. 5 (2015), 11431.
[12] J. Hyun, S.G. Lee, J. Hwang, Application of corona discharge-generated air ions for filtration of aerosolized virus and inactivation of filtered virus, J. Aerosol Sci. 107 (2017) 31–40.
[13] E. Kujundzic, M. Hernandez, S.L. Miller, Ultraviolet germicidal irradiation inactivation of airborne fungal spores and bacteria in upper-room Air and HVAC in-duct configurations, J. Environ. Eng. Sci. 6 (2007) 1–9.

[14] M. Buonanno, D. Welch, I. Shuryak, et al., Far-UVC light (222 nm) efficiently and safely inactivates airborne human coronaviruses, Sci. Rep. 10 (2020), 10285.
[15] M. Rodríguez, M.L. Palop, S. Seseña, A. Rodríguez, Are the Portable Air Cleaners (PAC) really effective to terminate airborne SARS-CoV-2? Sci. Total Environ. (2021), 147300.
[16] B. Blocken, T. van Druenen, A. Ricci, L. Kang, T. van Hooff, P. Qin, A.C. Brombacher, Ventilation and air cleaning to limit aerosol particle concentrations in a gym during the COVID-19 pandemic, Build. Environ. 193 (2021), 107659.
[17] E.S. Mousavi, N. Kananizadeh, R.A. Martinello, J.D. Sherman, COVID-19 outbreak and hospital air quality: a systematic review of evidence on air filtration and recirculation, Environ. Sci. Technol. 55 (7) (2021 Apr 6) 4134–4147.
[18] American Society of Heating, Refrigerating and Air-Conditioning Engineers, Core Recommendations for Reducing Airborne Infectious Aerosol Exposure, ASHRAE Epidemic Task Force, Atlanta, Georgia, USA, 2021. October 2021.
[19] Eng Kee Tristan Yeo, Kok Hing Chong, Tong Liong Basil Wong, Nee Shin Victor Bong, Man Djun Lee, Anak Boniface Christopher Jantai, Alternative design of air ventilation in passenger lift for thermal comfort, CFD Lett. 12 (1) (2020) 37–47.
[20] Ad Van Deer, R. Claessen, W. Van Der Spoel, P. Van der Velde, Downflow ventilation system ensures healthy and safe air in elevator cabins, REHVA Journal (2021) 71–78. June.
[21] C. van Rijn, G.A. Somsen, L. Hofstra, G. Dahhan, R.A. Bem, S. Kooij, D. Bonn, Reducing aerosol transmission of SARS-CoV-2 in hospital elevators, Indoor Air 30 (6) (2020) 1065–1066.
[22] M. Ereth, T. Wagoner, M. Blevins, D. Hess, Elevator cabin decontamination with active particle control technology, Front. Public Health 9 (2021), 729204.
[23] Z. Nouri, N. Norouzi, E. Ataei, S. Azizi, Virologic microparticle fluid mechanics simulation: COVID-19 transmission inside an elevator space, International Journal of Computational Materials Science and Engineering 10 (2) (2021) 2150007–2150588.
[24] Jiying Liu, Shengwei Zhu, Moon K. Kim, Jelena Srebric, A review of CFD analysis methods for personalized ventilation (PV) in, Indoor Built Environments *Sustainability* 11 (15) (2019) 4166.
[25] S. Ibrahim, R.C. Mehta, An investigation of air flow and thermal comfort of modified conventional car cabin using computational fluid dynamics, J. Appl. Fluid Mech. 11 (2018) 141–150. Special Issue.
[26] M. Cehlin, U. Larsson, H.J. Chen, Numerical investigation of air change effectiveness in an office room with impinging jet ventilation, in: Proceedings of the 4th International Conference on Building Energy, Environment. 5-9 Feb. Melbourne, Australia, 2018.
[27] A.M. Farag, E.E. Khalil, Numerical analysis and optimization of different ventilation systems for commercial aircraft cabins, in: 2015 IEEE Aerospace Conference, 2015, pp. 1–12.
[28] American Society of Heating, Refrigerating and Air-Conditioning Engineers, ASHRAE Handbook - Fundamentals, 2007 (Chapter 16): Ventilation & Infiltration. Atlanta, Georgia, USA.
[29] American Society of Heating, Refrigerating and Air-Conditioning Engineers, ANSI/ASHRAE Standard 62.1-2013. **Ventilation for Acceptable Indoor Air Quality**, 2013 (Atlanta, Georgia, USA).
[30] Vivian Chanteloup, Pierre-Sylvain Mirade, Computational fluid dynamics (CFD) modelling of local mean age of air distribution in forced-ventilation food plants, J. Food Eng. 90 (1) (2009) 90–103.
[31] Alberto Meiss, Jesús Feijó-Muñoz, A. Miguel, García-Fuentes, Age-of-the-air in rooms according to the environmental condition of temperature: a case study, Energy Build. 67 (2013) 88–96.
[32] Mao Ning, Mengjie Song, Mingyin Chan, Dongmei Pan, Shiming Deng, Computational fluid dynamics (CFD) modelling of air flow field, mean age of air and CO2 distributions inside a bedroom with different heights of conditioned air supply outlet, Appl. Energy 164 (2016) 906–915.
[33] S. Mazumdar, S. Poussou, C.H. Lin, S.S. Isukapalli, M.W. Plesniak, Q. Chen, The impact of scaling and body movement on contaminant transport in airliner cabins, Atmos. Environ. 45 (33) (2011) 6019–6028.
[34] J. Wang, T.T. Chow, Influence of human movement on the transport of airborne infectious particles in hospital, Journal of Building Performance Simulation 8 (4) (2015) 205–215.
[35] J. Hang, Y. Li, R. Jin, The influence of human walking on the flow and airborne transmission in a six-bed isolation room: tracer gas simulation, Build. Environ. 77 (2014) 119–134.
[36] European Normative EN-81-20, Safety Rules for the Construction and Installation of Lifts - Lifts for the Transport of Persons and Goods - Part 20: Passenger and Goods Passenger Lifts, 2020.
[37] American Society of Mechanical Engineers, ASME Standard A17.1/CSA B44. **Handbook on Safety Code for Elevators and Escalators**, 2007.
[38] R.D. Blevins, Applied Fluid Dynamics Handbook, Krieger Publishing, 1984.
[39] Z. Zhang, Z.Q. Zhai, W. Zhang, Q. Chen, Evaluation of various turbulence models in predicting airflow and turbulence in enclosed environments by CFD: Part 2 - comparison with experimental data from literature, HVAC R Res. 13 (2007) 871–886.
[40] ANSYS-FLUENT Meshing User's Guide, Release 15.0, ANSYS, Inc., 2013.
[41] G. Gan, H.B. Awbi, Numerical prediction of the age of air in ventilated rooms, in: Proceedings of 4th International Conference on Air Distribution in Rooms, 15-17 June, 1994. Krakow, Poland, 1994.
[42] J. Abanto, D. Barrero, M. Reggio, B. Ozell, Airflow modelling in a computer room, Build. Environ. 39 (2004) 1393–1402.
[43] K.M. Argüelles, J.M. Fernández Oro, M. Galdo Vega, E. Blanco, Effects of prong-wire interferences in dual hot-wire probes on the measurements of unsteady flows and turbulence in low-speed axial fans, Measurement 91 (2016) 1–11.
[44] M.L. Pollock, T. Hickman, Z. Kendrick, A. Jackson, A.C. Linnerud, G. Dawson, Prediction of body density in young and middle-aged men, J. Appl. Physiol. 40 (3) (1976) 300–304. Mar.